The Troublesome Broadband Evolution of GRB 061126: Does a Grey Burst Imply Grey Dust?

D. A. Perley[1], J. S. Bloom[1], N. R. Butler[1], L. K. Pollack[2], J. Holtzmann[3], C. H. Blake[4], D. Kocevski[1], W. T. Vestrand[5], W. Li[1], R. J. Foley[1], E. Bellm[6], H.-W. Chen[7], J. X. Prochaska[2], D. Starr[1], A. V. Filippenko[1], E. E. Falco[4], A. H. Szentgyorgyi[4], J. Wren[5], P. R. Wozniak[5], R. White[5], J. Pergande[5]

[1] Department of Astronomy, 601 Campbell Hall, University of California, Berkeley, CA 94720-3411.

[2] University of California Observatories - Lick Observatory, University of California, Santa Cruz, CA 95064

[3] Department of Astronomy, New Mexico State University P. O. Box 30001, MSC 4500, Las Cruces, New Mexico 88003-8001

[4] Harvard-Smithsonian Center for Astrophysics, 60 Garden Street, Cambridge, MA 02138

[5] Los Alamos National Laboratory, Los Alamos, NM, 87545

[6] U.C. Berkeley Space Sciences Laboratory, 7 Gauss Way, Berkeley CA 94720

[7] Department of Astronomy and Astrophysics, University of Chicago, 5640 S. Ellis Ave, Chicago, IL 60637

Received _____; accepted _____

ABSTRACT

We report on observations of gamma-ray burst (GRB 061126) with an extremely bright ($R \approx 12$ mag at peak) early-time optical afterglow. The optical afterglow is already fading as a power-law 22 seconds after the trigger, with no detectable prompt contribution in our first exposure, which was coincident with a large prompt-emission pulse. The optical-IR photometric SED is an excellent fit to a power-law but exhibits a moderate red-to-blue evolution in the spectral index at about 500 sec. This color change is contemporaneous with a switch from a relatively fast decay to slower decay. The rapidly decaying early afterglow is broadly consistent with synchrotron emission from a reverse shock, but a bright forward shock component predicted by the intermediate- to late-time X-ray observations under the assumptions of standard afterglow models is not observed. Indeed, despite its remarkable early-time brightness this burst would qualify as a dark burst at later times on the basis of its nearly flat optical-to-X-ray spectral index. Our photometric SED provides no evidence of host extinction, requiring either large quantities of grey dust in the host system (at $z = 1.1588 \pm 0.0006$, based upon our late-time Keck spectroscopy) or separate physical origins for the X-ray and optical afterglows. In either case, events like GRB 061126 may represent a significant fraction of observed dark bursts with faint or absent optical afterglows, suggesting a need for redress of the interpretations concerning the origin of these events, and possibly of afterglows in general.

Subject headings: gamma rays: bursts, gamma-ray bursts: individual: 061126

1. Introduction

While the study of the early-time X-ray afterglows of gamma-ray bursts (GRBs) has seen enormous strides since the launch of the *Swift* satellite (Gehrels et al. 2004), progress in the understanding of the longer-wavelength emission has been somewhat more limited. Early-time data from rapid-response telescopes are normally unfiltered, or different filters are observed nonsimultaneously, confusing spectral and temporal evolution. At later times, due to the large number of bursts now being detected and faintness of most afterglows, detailed photometry is no longer commonly acquired.

This is unfortunate, as a complete understanding of *Swift* afterglows can only come from a combined broadband picture that allows us to systematically investigate whether the peculiarities seen in X-ray data carry over into the optical domain. Many of the same questions raised by recent X-ray results can also be asked about the optical: Is there a prompt component of the emission, analogous to the steeply-decaying component seen in X-rays (Barthelmy et al. 2005)? Does the optical light curve show unusual features suggestive of energy injection such as the nearly-ubiquitous X-ray shallow-decay phase (Nousek et al. 2006)? Are there achromatic optical and X-ray breaks? Do the optical and X-ray afterglows even have a common origin at early times?

Previous studies have provided important hints. Most observations have been interpreted to support the consensus picture of synchrotron emission originating from a forward shock as it sweeps through the interstellar medium (e.g., Dai & Lu 1999, Vrba et al. 2000), or less commonly through a stellar wind (Price et al. 2002; Nysewander et al. 2006). In a smaller number of cases (Akerlof et al. 1999; Li et al. 2003a; Kobayashi & Zhang 2003; Shao & Dai 2005), very early-time data has provided tentative evidence for an additional emission component originating from the reverse shock as it travels backwards into the shocked material in the frame of the forward shock. Recently, studies of

early-time light curves have also shown evidence of significant delay between the onset of the prompt emission and the afterglow (Rykoff et al. 2004), and in at least one case complicated energy injection and explosive activity as late as nearly an hour after the gamma-ray burst (Woźniak et al. 2006), long after the gamma-ray emission has faded away. However, simultaneous, correlated optical and gamma-ray emission has also been reported (Blake et al. 2005; Vestrand et al. 2005, 2006; Yost et al. 2006) for some events. In the *Swift* era, comparison to the very early X-ray afterglow has also been of great interest (e.g., Quimby et al. 2006).

Most interpretations of the early afterglow have been based on unfiltered observations, or observations in a single filter. Without information about the frequency domain, the reported early-time behaviors discussed above are difficult to definitively associate with any single physical interpretation. Fortunately, the increasing number of fast-responding robotic ground-based observatories, the maturation of existing ones, and the rapid-response capabilities of *Swift* are beginning to address this observational gap.

In the following discussion, we report on one of the brightest bursts of the *Swift* era, GRB 061126. The breadth and rapidity of the ground-based response to this burst were remarkable, including unfiltered detection during the prompt emission and multi-color simultaneous detections in filters from U through K_s (ranging a full decade in frequency space) starting at less than one minute after the burst trigger. This data set allows the opportunity to examine in unprecedented detail the time-dependent color properties of an early GRB afterglow.

In §2 we present our observations from IR through gamma-rays of the early afterglow and our late-time Keck spectrum of the host, establishing the probable redshift of this system to be $z = 1.1588$. In §3.1 we examine the properties of the prompt emission, and show that the high-energy and optical emission are observationally uncorrelated temporally

or spectrally even at very early times. In §3.2-3.3 we examine the properties of the optical/IR light curve, and provide evidence for a red-to-blue change in the spectral index of $\Delta\beta \sim 0.3$ at early times. We investigate the X-ray behavior in §3.4, and show that no standard adiabatic model can fully explain the behavior seen by the XRT. Finally, while in §3.5-3.6 we show that the earliest afterglow appears reasonably fit by a reverse shock and the later afterglow by a forward shock based on the optical data alone, in §3.7 we demonstrate that an extrapolation of the X-ray spectrum overpredicts the contemporaneous optical flux by a factor of 5–20. We demonstrate using the optical-IR SED that this discrepancy cannot be due to any known dust extinction law. Unless we appeal to large quantities of grey dust, we argue in §4 that the X-ray and optical afterglow emission from this burst may have separate physical origins, suggesting a need for a major revision of standard assumptions for the origin of at least some GRB afterglows.

2. Observations

2.1. Swift BAT and XRT

At 08:47:56 UT, the *Swift* Burst Alert Telescope (BAT) triggered and located GRB 061126. Unfortunately, due to an Earth-limb constraint, *Swift* was unable to slew promptly to the target for 23 minutes and did not begin observations with the XRT or UVOT until that time. After 23 minutes, *Swift* slewed to the burst position and detected a fading X-ray afterglow (Sbarufatti et al. 2006a).

We download the *Swift* BAT and XRT data from the *Swift* Archive[1]. The XRT data are processed with version 0.10.3 of the `xrtpipeline` reduction script from the HEAsoft 6.0.6[2]

[1]ftp://legacy.gsfc.nasa.gov/swift/data

[2]http://heasarc.gsfc.nasa.gov/docs/software/lheasoft/

software release. We employ the latest (2006-12-19) XRT and BAT calibration files. We establish the BAT energy scale and mask weighting by running the `bateconvert` and `batmaskwtevt` tasks, also from the HEAsoft 6.0.6 software release. BAT spectra and light curves are extracted with the `batbinevt` task, and response matrices are produced by running `batdrmgen`. We apply the systematic error corrections to the low-energy BAT spectral data as advised by the BAT Digest website[3]. The spectral normalizations are corrected for satellite slews using the `batupdatephakw` task.

The reduction of XRT data from cleaned event lists output by `xrtpipeline` to science ready light curves and spectra is described in detail in Butler & Kocevski (2007). The XRT, BAT, and RHESSI data are fit using ISIS[4].

2.2. RHESSI

RHESSI (Lin et al. 2002) is a dedicated solar observatory which uses nine Germanium detectors to image the Sun at hard X-ray to gamma-ray energies (3 keV – 17 MeV). These detectors are unshielded and therefore frequently detect emission from off-axis GRBs. GRB 061126 was detected by RHESSI, which with its large spectral range allows us to complete the high-energy spectrum of this event.

To model the RHESSI response to off-axis photons, we have used Monte Carlo simulations and a detailed mass model. Since RHESSI rotates about its axis with a 4-second period, we have generated azimuthally-averaged responses spaced 15 degrees apart in polar angle. These responses are 2D matrices of effective area: input photon energy vs. detected count energy bins. At present both energy axes are 64 logarithmic bins from 10 keV to 10

[3]http://swift.gsfc.nasa.gov/docs/swift/analysis/bat_digest.html

[4]http://space.mit.edu/CXC/ISIS/

MeV. We generate the response matrices with `MGEANT` simulations: each response requires 64 simulations of a monoenergetic input spectrum, one for each photon energy bin. For an individual GRB, we generate and subtract a background count spectrum using data intervals before and after the burst. We generate a burst-specific response matrix with a weighted average of the two adjacent 15-degree responses. Convolving a spectral model with the response yields a model count spectrum for fitting to the GRB data.

2.3. RAPTOR

RAPTOR-S is an 0.4-m, fully autonomous robotic telescope, typically operated at focal ratio f/5. It is equipped with a 1k × 1k pixel CCD camera employing a back-illuminated Marconi CCD47-10 chip with 13 μ pixels. The telescope is owned by Los Alamos National Laboratory and located at the Fenton Hill Observatory (106.67° W, 35.88° N) at an altitude of ∼2500 m in the Jemez Mountains of New Mexico.

The RAPTOR-S telescope responded to the *Swift* trigger at 08:48:17.29 UT, 20.87 s after the trigger and 4.3 seconds after receiving the GCN packet. The telescope took a series of nine unfiltered 5-second exposures (the first two of which occurred while detectable gamma-ray emission was still ongoing), followed by a series of 10- and 30-second exposures. The optical transient is detected in all these frames. Preliminary photometric calibration was performed using the R-band magnitudes from the USNO B1.0 catalog. However, for consistency with the unfiltered KAIT observations (which were calibrated using the more precise SDSS measurements), we subtract a constant offset of 0.16 magnitudes post-calibration.

The RAPTOR photometry (not including this final offset) is given in Table 1.

2.4. PAIRITEL

Starting in 2003, we began to automate to the 1.3 meter telescope, formerly used for 2MASS (Skrutskie et al. 2006), on Mt. Hopkins, Arizona. The telescope was re-outfitted with the Southern 2MASS camera and all the control and data acquisition systems were rewritten from scratch (Bloom et al. 2006b). One of the primary science drivers was for rapid followup to *Swift* bursts. Since the camera obtains images every 7.8 sec simultaneously in three IR bands (J, H, K_s) and IR wavelengths are relatively immune to extinction, the PAIRITEL project was developed to provide complimentary insight into the nature of the early afterglow and to constrain dust (or neutral hydrogen at high redshift) extinction along the lines-of-sight. By September 2006, we had observed 81 *Swift* and INTEGRAL bursts starting several minutes to days after the bursts. The previous record response was with GRB 051109A ($t = 1.5$ minutes after the satellite trigger) (Bloom 2005) but other sub-10 min responses have also been fruitful (e.g., 050509B: Bloom et al. 2006a; 041219A: Blake et al. 2005).

At 08:48:18 UT ($t = 22$ sec), our customized Python-based client to the GCN socket server[5] was triggered with the GCN/SWIFT_BAT_POSITION message of GRB 061126. The autonomous slew of the telescope and dome began at 08:48:22 and ended at 08:48:47; the slew time was short since we had been observing M82 (23.9° to the east of the GRB) immediately prior to the GRB. After an initial reset of the camera, the first 7.8 second images in J, H, and K_s bands were obtained starting at 08:48:54.35 UT ($t = 58$ sec). We continued with a dense sampling of observations over the next three hours as well as several hours of imaging the following night.

[5]These software is freely available with a GNU public license: https://sourceforge.net/projects/pygcnsock/

Reductions of the individual images were performed using a set of customized scripts written in PYRAF and Python. The afterglow was well-detected ($> 10\sigma$ S/N) in individual images for the first 20 minutes of observations (Figure 1). In fact, the H and K_s band fluxes of the afterglow are so bright in the first few minutes that the pixel responses were in the non-linear regime. Unfortunately the cloud cover in Arizona was highly variable during the first thirty minutes of GRB 061126 observations, leading to variable transmission on 10 second timescales.[6] As such, in our analysis we refit the zeropoint in every individual exposure to the 2MASS catalog. The typical rms uncertainty in the zeropoints are 2–3%. Given the large variations in the sub-pixel response function for NICMOS3 arrays we have found that aperture photometry on individual exposures inheres a roughly 3% systematic uncertainty from image to image (Blake et al. 2007, in preparation). Table 2 gives the aperture magnitude measurements from the PAIRITEL observations. In this table and in all plots and modeling, we exclude exposures in which the CCD response was nonlinear, as well as H-band observations during periods of poor transmission.

2.5. NMSU 1m

Optical observations in the Johnson-Cousins *UBVRI* filters were obtained using the New Mexico State University robotic 1m telescope located at Apache Point Observatory. Because the telescope happened to be pointed relatively near the burst location, the first observations were started only 47 seconds after the burst trigger, and only 31 seconds after the alert. The telescope took five sequences of observations in the order I, R, V, B, U with exposure times 10, 10, 20, 40, and 60s, respectively, then took another five sequences

[6]An animated image showing the variable transmission and fading afterglow can be viewed at http://lyra.berkeley.edu/~jbloom/grb061126a-hband.mpg

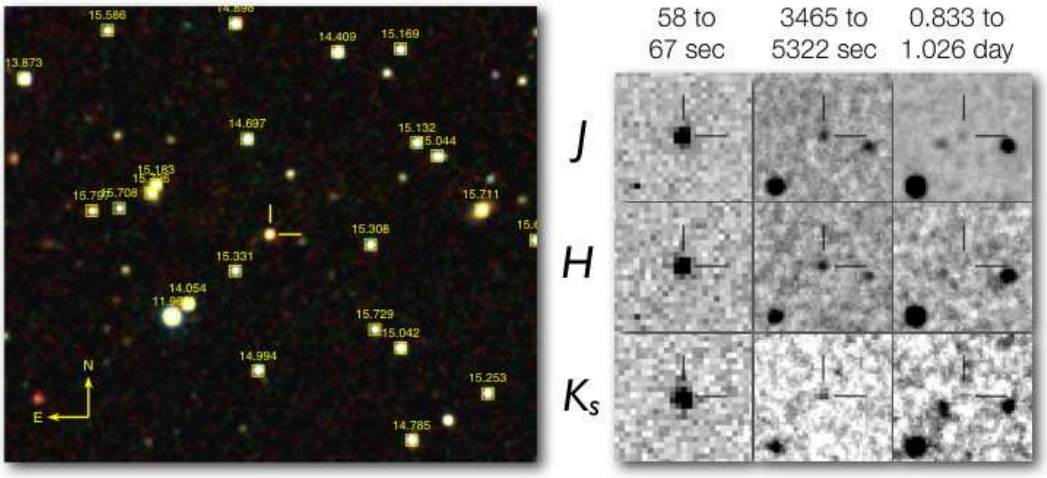

Fig. 1.— False-color PAIRITEL finding chart ($260'' \times 260''$) of the afterglow of GRB 061226. The 2MASS catalog magnitudes of stars used for the photometric calibration are denoted with boxes at the catalog position and the J-band (2MASS) magnitude. At right, images showing the fading of the afterglow from 58 seconds to 1 day after the GRB. Images are progressively deeper at each epoch.

of observations with exposure times 20, 20, 40, 80, and 120s; with overhead, these ten sequences took about an hour to complete. The afterglow was detected in all of the observations, with random error ranging from better than 0.01 mag in the first series to 0.1–0.2 mag in the last series.

The afterglow brightness was measured using aperture photometry with an aperture of $3''$ radius; several reference stars in the field were also measured. Calibration was achieved via observations of these reference stars, along with *UBVRI* standard stars, on the night of 21/22 December 2006. A standard photometric solution was derived for this night, yielding calibrated magnitudes for the reference stars. On the calibration night, the standard star solution yield RMS deviations of about 0.03 mag in each bandpass, so the calibration zeropoints are accurate only to this level.

The final photometry is given in Table 3.

2.6. KAIT and Lick 1.0m

The 30-inch robotic Katzman Automatic Imaging Telescope (KAIT, Filippenko et al. 2001) and its GRB alert system (Li et al. 2003b) responded to the GCN notice with the position of GRB 061126 at $t = 16$ s, and attempted to execute a pre-arranged observation sequence. Unfortunately, the weather conditions were poor, so KAIT did not acquire a useful image until $t = 305$ s. Also, the telescope did not have a successful focusing procedure before the GRB observations (again due to bad weather), so the images were not fully in focus. Nevertheless, a sequence of V, I, and unfiltered observations were made, and the GRB afterglow was detected on most images. A successful focusing procedure was executed during the middle of the GRB observations, and KAIT followed the GRB until the humidity forced the system to shut down at $t \sim 1.8$ h. The images were automatically processed with the proper dark current, bias, and flat fields before measuring photometry, calibrating relative to ten SDSS stars (Cool 2006). The reference magnitudes of these stars were converted to VRI using the transformation equations of Lupton (2005)[7]. Unfiltered observations were calibrated using the R-band magnitudes.

A sequence of 300 s R-band images were also manually observed at the Lick Observatory Nickel 1-m telescope from $t \sim 1.0$ h to 1.7 h. The observations were again terminated due to the weather conditions. The images were manually reduced with the proper calibrations files (bias, dark current, and flat field images), and calibrated relative to our SDSS reference stars. The photometry is given in Table 4.

[7]http://www.sdss.org/dr4/algorithms/sdssUBVRITransform.html#Lupton2005

2.7. Swift UVOT

Swift began follow-up observations of GRB 061126 at 1605 seconds after the burst trigger, its slew having been delayed as a result of the Earth-limb constraint. Despite this time delay the afterglow was still detected, albeit marginally, in all of the UVOT filters except for UVW2.

We acquired the UVOT imaging data from the NASA archive[8]. Unfortunately the afterglow had already become quite faint by the beginning of the observations, and is not well-detected except in stacked exposures. To calculate the most accurate photometry possible, we therefore bin closely temporally spaced observations, and perform aperture photometry using the optimal aperture size as given in the prescription in Li et al. (2006) for the V, B, and U data. For the UV filters, we use the photometry reported by the UVOT team in the most recent GCN Report for this burst (Sbarufatti et al. 2006b). Our photometry is given in Table 5.

Despite our small-aperture analysis, the *UBV* photometry has large uncertainties, and some points are not formally consistent with effectively simultaneous ground-based observations in the same filters. This is not necessarily surprising; due to the extremely faint nature of the afterglow by the time that *Swift* completed its slew, the actual uncertainty on these measurements may be significantly larger than the nominal photometric error. We do not use these points in our modeling, but we do include them in our plots. The UVW1 and UVM2 points have even larger uncertainties (0.4–0.8 mag), no ground-based calibration is available, and Galactic extinction (which is significant in this direction: $A_{UVM2} \sim 1.8$ mag) is increasingly uncertain towards these wavelengths. Therefore we exclude these points from the formal fits as well, and restrict our modeling to the much more precise ground-based

[8]http://heasarc.gsfc.nasa.gov/docs/swift/archive/

photometry. However, we do include the UV points in our SED plots for comparison.

2.8. GCN Circulars

For comparative purposes, our plots also include points from the GCN circulars[9]. We do not actually use these points in our fitting. Most early-time data were calibrated against the USNO B1.0 survey (Monet et al. 2003), which does not contain very accurate photometry. Some data points were also calibrated against a preliminary release of an SDSS pre-burst observation of this field (Cool et al. 2006) which was later found to be incorrectly calibrated (indeed, our own use of these observations for our preliminary calibrations exposed the problem and motivated the re-release of the SDSS calibration used for the KAIT reductions, Cool 2006.) Therefore we include these points only for visual purposes but exclude them from the modeling. The photometry is summarized in Table 6.

2.9. Keck Host Imaging and Spectroscopy

The galaxy hosting GRB 061126 was observed during UT 18 January 2006 with the Low Resolution Imaging Spectrometer (LRIS) on Keck I. Using the 1.0″ longslit, the 600 mm^{-1} (λ_{Blaze} = 7500 Å) grating, and the 300 mm^{-1} (λ_{Blaze} = 5000 Å) grism, we obtained spectra covering the wavelength regions from 6680 to 9266Å and from 3200 to 7649Å with the red and blue cameras respectively. These data represent a total integration time of 40 minutes, split into two 20-minute exposures. The slit position and deep imaging of the field can be seen in Figure 2.

[9]http://gcn.gsfc.nasa.gov/gcn3_archive.html

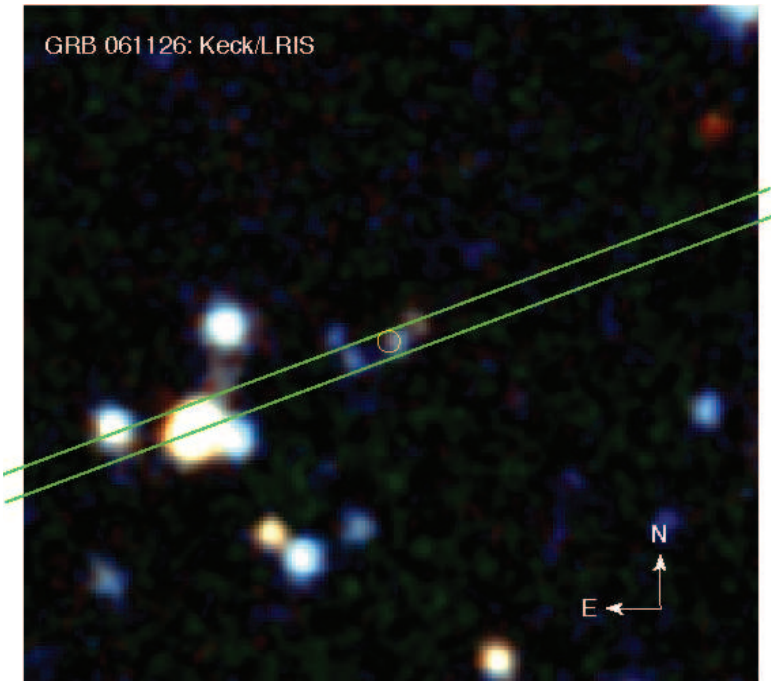

Fig. 2.— Keck (LRIS) late-time finding chart. The image is 25″ on a side and represents the stacked g' and R band. The placement of the 1″-wide slit is shown in green. The white circle is 2 sigma position of the afterglow as measured from PAIRITEL imaging. The probable host galaxy is visible at this location. The object is blue and extended, appearing to have a complicated morphology. Further down the slit 21.1″ to the southeast is a relatively bright galaxy with a redshift of $z = 0.6225 \pm 0.0004$, based on emission from [OIII] 5008.2 and 4960.2, from H_β, and from [OII] 3727.11 and 3729.86. (This galaxy is not associated with the GRB.)

The data were processed with an IDL package[10] customized for LRIS longslit reductions developed by J. Hennawi and J.X. Prochaska. In brief, the code bias subtracts and flattens each image with standard procedures. The code then identifies the edges of the longslit to define the scientific region. It automatically generates a wavelength solution down the

[10]Specifically, the Longslit codes now bundled within XIDL, http://www.ucolick.org/~xavier/IDL/index.html.

center of the slit by extracting and fitting to the CdZnNeAr spectrum. This wavelength solution is propagated throughout the entire 2D spectrum by tracing the curvature of the arc lines. The scientific data is sky subtracted by a bspline fit to the sky pixels. These are defined as all pixels not associated with the objects in the slit (found automatically by averaging the data in the spectral direction). A sky image is generated for the entire frame and subtracted. Each object identified within the slit is optimally extracted and a variance array is generated assuming Poisson statistics and read noise. A sky spectrum is also extracted for each object and cross-correlated against an archived sky spectrum to calculate a shift in the wavelength solution due to flexure in the LRIS instrument (typically on the order of ≈ 2 spectral pixels). The code then converts from air to vacuum wavelengths and shifts to heliocentric velocities. The spectra from multiple exposures are coadded, weighting by the median S/N and (since the night was photometric) fluxed using a spectrophotometric standard observed on 18 January 2006. In the case of GRB 061126, the galaxy was too faint to be automatically identified by these algorithms. Therefore, we directed the code to extract the data at the predicted position (determined from our imaging data) using the trace and spatial profile derived from the nearest object along the slit.

The two-dimensional reduced spectra show a faint blue continuum and a sole emission feature at ~ 8050Å (Figure 3). From the one-dimensional spectrum it is clear that the emission feature is slightly resolved; it has a FWHM of roughly 10Å, while the spectral resolution in that wavelength range, as determined by the FWHM of arc line profiles, is 5.8Å. As we detect only one emission feature, it is impossible to definitively report the redshift of the GRB host. However, the width of the line and the presence of obvious continuum blueward of this feature suggest that it likely corresponds to the [OII] $\lambda\lambda$ 3727.11, 3729.86Å doublet, implying that the GRB host lies at a redshift of $z = 1.1588 \pm 0.0006$. The width of the emission feature is consistent with an [OII] doublet at this redshift (3.19Å separation at $z = 1.159$) when convolved with the instrumental resolution. Furthermore,

if the emission is from [OII] we would not expect to see any other spectral lines; the most common, redder lines would fall redward of our red spectrum, and the only strong emission line blueward of [OII] is Lyα which lies below our spectral coverage. A less likely scenario is that the emission feature corresponds to a dynamically-broadened Lyα line in a host galaxy at $z = 5.6$, but the blue continuum flux that extends to $\lambda \sim 4890$Å would require an unlikely source of emission (e.g. a gravitationally lensed, blue background galaxy).

Adopting the 8050Å emission feature as the [O II] doublet, we can estimate the star formation rate (SFR) of the host galaxy based on the flux in these lines. We measure the total flux from the extracted, one-dimensional spectrum in the region between 8042.0 and 8056.0Å. (These wavelengths correspond to a 3σ region around each doublet line.) We measure the continuum by computing the median flux in two regions free of sky lines (regions "C" in Figure 3.) The total flux in these lines is $(1.6 \pm 0.2) \times 10^{-17}$ ergs s^{-1} cm^{-2}. Using the relation between [OII] luminosity and SFR described in Kennicutt (1998), we find that the GRB host galaxy is undergoing star formation at a rate of 1.6 ± 0.2 M$_\odot$ yr^{-1} (assuming $H_\circ = 71$ km s^{-1} Mpc^{-1}, $\Omega_{\rm M} = 0.3$, $\Omega_\Lambda = 0.7$, as we will throughout this paper). The intrinsic uncertainty in the calibration converting [O II] line luminosity into SFR is approximately 30% (Kennicutt 1998); this uncertainty is not included in our quoted error. Though our measured SFR must be considered a lower limit because we have not accounted for dust extinction, it is interesting to note that the rate of star formation in the host galaxy of GRB 061126 is comparable to the SFRs found in other GRB hosts, measured using dust-corrected UV fluxes as well as [O II] luminosities (Christensen et al. 2004).

3. Analysis and Discussion

3.1. Prompt Emission

The prompt emission from GRB 061126 displays a complex, multi-peaked profile dominated by two large pulses (Figure 4). After a gradually increasing component starting at 7 seconds before the trigger and a small precursor spike at $t \approx 1$ sec after the trigger, the first and largest pulse begins at $t \approx 3$ sec, and fades to about twice the background level by $t \approx 15$ sec. A second pulse begins at $t \approx 19$ sec, lasting until $t \approx 25$ sec. There is short-time microstructure in both pulses. The full burst has a T_{90} (Kouveliotou et al. 1993) of 25.75s in the full *Swift* 15-350 keV band.

Using the combined Swift BAT and RHESSI spectrum, we fit a Band model (Band et al. 1993) over several different time regions: The entire burst, the first pulse, and the second pulse. Results are summarized in Table 7. For the full burst, we measure an average peak energy $E_{p,obs}$ of 620 keV, though there is good evidence for hard-to-soft spectral evolution, as evidenced by the significantly different values of $E_{p,obs}$ during the two pulses. The total fluence over the full spectral range is $(3.0 \pm 0.4) \times 10^{-5}$ erg cm^{-2}, which at the putative host redshift of $z = 1.16$ corresponds to an isotropic release of energy of $E_{iso} = (1.06 \pm 0.14) \times 10^{53}$ erg over a 1-1000 keV host-frame bandpass, assuming our standard cosmology.

Given this value of E_{iso}, the Amati relation (Amati et al. 2002) predicts $E_{p,obs} = 130 \times 10^{0.0 \pm 0.3}$ keV, which is 2σ from the measured value. Given E_{iso} and $E_{p,obs}$, the Ghirlanda relation (Ghirlanda et al. 2004) predicts a jet break at $t = 10^{1.41 \pm 0.27}$ days (13-49 days). The beaming corrected energy release is $10^{51.6 \pm 0.2}$ erg, for a jet opening angle of $10^{1.21 \pm 0.10}$ degrees (13-20 degrees).

RAPTOR detected GRB 061126 contemporaneously with the BAT emission.

Fortuitously, the first unfiltered exposure (which took place from 20.87-25.87 seconds after the BAT trigger) matches quite well the second pulse of the GRB (peak time of 22.5 seconds and a T_{90} of about 5 seconds) – see the first optical point of Figure 4.

Comparing this first, contemporaneous data point to later exposures in which the prompt emission has faded, the early-time RAPTOR data are seen to fade as a simple power-law ($F_\nu \propto t^{-\alpha}$), with the decay index $\alpha \approx 1.5$ (using the GRB trigger time as t_o). There is no evidence for an additional prompt flux component based on an extrapolation backwards from later measurements. Consistent with this observation, if we extrapolate the best-fit Band model of the second GRB pulse into the optical (Figure 5), the predicted optical flux is only 250 μJy, significantly less than what is observed. Finally, if we extrapolate the Band model of the prompt emission in time to 60 seconds (assuming continued hard-to-soft spectral evolution and fading), it both falls far short of our multi-color data at that time and also has a different spectral slope (open circles and dashed line in Figure 5). For this burst, there is no clearly observable association between the prompt emission and the long-wavelength afterglow, even as early as 20 seconds after the burst. This is not inconsistent with earlier reports of a link: more likely, as our SED shows, the prompt component is simply dominated by an extremely bright early-time afterglow.

3.2. Optical Light Curve

While the very early optical light curve appears to follow a power-law behavior, the light curve enters a more complex phase within minutes. A brief visual inspection of the overall afterglow light curve (Figures 6 and 7) shows several interesting features of this burst. The early decay that began in our earliest data continues with the same trend for several decades in time, fading roughly as a power-law with an average α of about 1.5.

A simple power-law is clearly a poor fit, however, due to the presence of of a prominent "bump" feature at around 120 seconds.

Rapid early decay gives way to a shallower-decaying ($\alpha < 1$) component starting at about 10^3 seconds that dominates for the rest of our observations. Reports from the GCNs indicate an apparent steepening at later times, though with different authors disputing the value of the decay index: Rol et al. (2006) claim to observe $\alpha = 1.0 \pm 0.1$ between 0.54 and 1.76 days, though Pozanenko et al. (2006) report $\alpha = 1.5 \pm 0.13$ between 0.45 and 0.59 days, and Misra (2006) observe $\alpha \approx 1.4$ between 0.41 and 0.56 days.

In our modeling, we construct the light curve as a sum of several broken power-law components, each of generally different color as well as different decay indices.

$$F_\nu(t) = \sum_{j=0}^{n} F_{\nu,j} \left[\left(\frac{t}{t_{\nu,j}} \right)^{\alpha_{j,b} s} + \left(\frac{t}{t_{\nu,j}} \right)^{\alpha_{j,a} s} \right]^{-1/s}$$

The flux offset $F_{\nu,j}$ generally depends on the filter (represented by the subscript ν) as well as on the component (j). The temporal decay index α depends on the component and whether or not it is before the break (subscript b) or after (subscript a) but not the frequency. The broken power-law model is that of Beuermann et al. (1999).

Numerous models, in which certain parameters were fixed or free to vary, were experimented with. Each model uses the same three components:

1. The first component (henceforth the "fast" component) is modeled as a decaying power-law, with no break ($\alpha_{F,a} = \alpha_{F,b}$).

2. On top of this, we add an early "bump" component. As the bump appears very early and is sampled from beginning to end only in RAPTOR-clear and PAIRITEL J-band, its color cannot be well-constrained, so it is fixed to be the same color as the fast

component ($F_{\nu_B} = C_B F_{\nu_F}$, where C_B is a single filter-independent fit parameter, and $t_{\nu,B} = t_B$). The rising index is fixed at $\alpha_{B,b} = -0.5$ and its sharpness s is fixed at 1.0; other parameters are free to vary. (This bump feature is included for empircal reasons and to be sure we do not bias the sparsely sampled early optical SED, not necessarily because its origin is physically distinct. It could also be caused by, for example, a density variation modulating the fast component.)

3. At later times, we add a third "slow" component. The break time, pre- and post- break temporal indices, and the pre- and post- break spectral indices of this component are fixed (or allowed to vary) depending on the physical or empirical model.

Note that all of our models assume the features described in (1) and (2), above, differing only in the treatment of the slow component. The values of the fit parameters for the first two components are allowed to vary to reach their best-fit value under each model.

Our data only trace the light curve with no gaps in coverage until ≈ 7000 seconds, and we have no color information past 4000 seconds aside from a marginal J band detection and H and K_s limits from the second night. Later-time measurements are present in the GCN circulars, but different authors report different and somewhat contradictory behavior, suggesting either a problem with some of the public data or complex behavior of the light curve at late times. As a result, we do not include any optical points after 10^4 seconds in our fits, anticipating that the late-time optical evolution will be discussed in greater detail in upcoming work by Mundell et al. Instead, we focus on the properties of the early and intermediate afterglow.

The first class of models are purely empirical and assume a late-time power-law with no break, except possibly at late times (beyond the coverage of our data). The decay index of this power-law (α_S) is in all cases free to vary. We do not directly constrain the spectral index (defined here using the convention $F_\nu \propto \nu_{eff}^{-\beta}$) or require a power-law spectral

energy distribution. However, in some models we do constrain the change in the spectral properties. In our different models, these color constraints are as follows: (a) unconstrained, allowing the linear flux factor $F_{\nu,S}$ to take arbitrary values for each filter, (b) constrained as to allow no spectral evolution: $F_{\nu,S} = CF_{\nu,F}$, or (c) constrained in such a way as to permit the spectral index of the slow component to differ from that of the fast component by $\Delta\beta_{F-S}$ by fixing $F_{\nu,S} = CF_{\nu,F}(\nu/\nu_{R-band})^{-\Delta\beta_{F-S}}$. Note that this *difference* in the spectral index can be fit directly regardless of Galactic extinction (which is significant) or host extinction (which is likely not, as we will discuss later) as long as the extinction can be assumed to be a constant with respect to time.

The final model is theoretically motivated, modeling the slow component as a forward shock whose flux peaks at some time during our multicolor observations. The slow component's rising and decay indices ($\alpha_{S,b}$ and $\alpha_{S,a}$, respectively) and the change in spectral index across the break $\Delta\beta_S$ are fixed using the constraints from the X-ray spectrum discussed in §3.4. This model is described in more detail during our discussion of the forward shock in §3.6.

In all cases, after fitting we correct for Galactic extinction of $E_{B-V} = 0.182$ (using the NED extinction calculator[11], Schlegel et al. 1998) and fit a simple power-law to estimate the observed spectral index for different components. (This neglects the possibility of host extinction, but as we will show in §3.7 if host extinction is present it does not cause significant deviation from a power-law.)

Despite the complexity of the models, no fit is observed to give a value of $\chi^2/\mathrm{dof} \sim 1$.

[11]The NASA/IPAC Extragalactic Database (NED) is operated by the Jet Propulsion Laboratory, California Institute of Technology, under contract with the National Aeronautics and Space Administration.

The most successful model, using unbroken power-laws and arbitrary filter-dependent color change, gives $\chi^2/\mathrm{dof} \sim 6$. This is not surprising; modulations in afterglow flux have been observed in many previous cases (for example, Lipkin et al. 2004). Accordingly, we add in quadrature an extra uncertainty of 0.08 magnitudes to all the photometric measurements. With this adjustment, our different models give fit results as given in Table 9. There is strong evidence for color change — a fit allowing no change in the relative fluxes of different components has a value of $\chi^2/\mathrm{dof} = 261.9/193$, while an equivalent fit allowing the early fast-fading and later slow-fading components to have different spectral indexes (Figure 8) gives $\chi^2/\mathrm{dof} = 231.3/192$. Under this model, β shifts towards the blue across the transition by $\Delta\beta_{F-S} = -0.383 \pm 0.075$.

3.3. Optical Color Evolution

The above results indicate color evolution across the steep-to-shallow transition. To confirm this behavior and ensure this is not an artifact of the modeling, we construct truly contemporaneous SEDs using simultaneous PAIRITEL and NMSU 1.0m observations by mosaicing only those individual PAIRITEL exposures taken during the NMSU exposure time range. In cases where the exposure time is much less than the time since the burst, we add a small amount of additional buffer time before and after the start and end of the optical exposures since the signal to noise at late times was quite low. After correcting for Galactic extinction, we fit the three $J/K_s/$[optical] data points with a basic power-law, and determine the best-fit value and uncertainty for the spectral index β. (We omit H-band measurements from this fit, since the variable transmission introduces a significantly larger scatter in that band compared to J and K_s.) The results are plotted in Figure 9.

These are consistent with a color change. The early-time colors from the first NMSU filter cycle are consistent with a spectral index of $\beta = 1.2 \pm 0.1$, but starting at around

500 seconds the colors shift notably blueward and at later times the index is typically $\beta = 0.95 \pm 0.10$. This provides model-independent support of our fit conclusion that the afterglow has undergone a color change.

3.4. X-ray Light Curve and Closure Constraints

Due to the complex behavior of the optical light curve and the possibility of host extinction, it is difficult to apply any constraints on the physical parameters of this burst from the optical observations alone. However, in principle the degeneracy can be broken using the XRT data. The XRT light curve (Figure 6) fades as a purely unbroken power-law with a decay index $\alpha_X = 1.31 \pm 0.01$ over the entire span of the *Swift* observations, from ∼2 ksec out to nearly 10 days. (For the fit, $\chi^2/\mathrm{dof} = 668.2/550$). After removing the effect of neutral hydrogen absorption (both Galactic, for which we estimate $N_{\mathrm{H,Galactic}} = 0.103 \times 10^{22}$ cm^{-2} from Dickey & Lockman (1990), and at the host redshift, for which we calculate a best-fit value of $N_{\mathrm{H,host}} = 1.1 \pm 0.3 \times 10^{22}$ cm^{-2}), the X-ray spectrum is a good fit ($\chi^2/\mathrm{dof} = 213.9/238$) to a simple power-law, with a spectral index $\beta_X = 1.00 \pm 0.07$. There is no evidence for spectral evolution during the observations: using the X-ray hardness ratio (see Butler & Kocevski 2007), we constrain the change in the X-ray spectral slope to be $\Delta\beta_X < 0.4$ (90% confidence). Our analysis is consistent with that from the most recent GCN report for this event, Sbarufatti et al. (2006b).

We use the closure relations of Price et al. (2002), as derived from the predictions of the spectrum of an afterglow by Sari et al. (1998) to attempt to constrain the environment (constant-density ISM, wind-stratified medium, or an expanding jet) and the location of the cooling break (redward or blueward of the X-ray frequency range). Surprisingly these values of α and β are not consistent with any of the standard closure relations (Table 8). Only the ISM-B model, for a uniform-density medium where the cooling break is blueward

of the X-rays, is consistent within 2σ. However, this regime is unlikely to be appropriate. First, the optical data are clearly decaying at a substantially slower rate. If the cooling break has not yet passed through the X-ray, it will not have passed through the optical either in an ISM medium. Second, such a late ($\gtrsim 10^6$s) cooling break in the X-ray band would imply an extremely low density ($\ll 1$ cm^{-3}), inconsistent with a galactic environment and the high N_H column density observed in the X-ray data. (A column depth of 1 kpc predicts $\rho > 4$ cm^{-3} if the gas is uniformly distributed throughout the galaxy.)

If we admit closure relations within 3σ, then the Wind-R and ISM-R models become admissible. Of these, only the ISM model is consistent with the observed slower optical decay: in a wind-driven medium, the cooling break moves blueward, and so (as with the ISM-B case) we expect the X-ray and optical to have the same or nearly the same decay slope.

As a result, we take the ISM-B case as our best model. However, the lack of closure is clearly significant and indicates that at least one standard assumption does not hold. A few possibilities could help explain the discrepancy:

1. The environmental profile is neither constant nor that of a stellar wind (that is, the parameter k in $\rho \propto r^{-k}$ is not 0 or 2). However, as long as $\nu_X > \nu_c$, which we argue above is almost certainly the case at these late times, the closure relation is indepdendent of environment, so this is not a likely possibility.

2. The afterglow evolution is dominated by radiative losses and has not yet transitioned to an adiabatic phase, even out to ~ 9 days. The appropriate closure relation for this case is $C = \alpha - 12\beta/7 + 2/7 = -0.119 \pm 0.120$. This is within 1σ of the expected value of 0. However, this requires that the synchrotron spectrum still be fast-cooling, which generally implies a rising optical light curve; this is not observed. If we allow the optical frequency to be above the synchrotron critical frequency ($\nu_{opt} > \nu_o$), then

a fading optical light curve with $\alpha = 4/7 = 0.57$ can be produced.

3. The X-ray light curve is affected by synchrotron self-Compton losses, which would steepen the decay slightly relative to that predicted by a no-Compton model (Sari & Esin 2001). The amount of predicted steepening is unfortunately relatively low: $\Delta\alpha \sim 0.5(p-2)/(4-p)$, which for the X-ray inferred value of $p = 2\beta = 2.0 \pm 0.14$ give a constraint of the SSC-corrected decay index of 1.0 ± 0.14, still off by 2σ from the observed value of 1.31 ± 0.01.

4. The X-ray emission is not due to a forward shock, or not due to synchrotron radiation.

Some combination of factors may also be at work. In any event, the specific resolution to the closure problem is not critical at this stage. For now, we need only assume that the X-ray photons originate from post-cooling break electrons to proceed with our predictions for the optical light-curve behavior. The X-ray spectral index of $\beta = 1.00 \pm 0.07$ corresponds to an electron index of $p = 2.00 \pm 0.14$, the minimum value for an distribution that is unbroken at high energies.

3.5. The Very Early Afterglow Decay - a Reverse Shock?

For any assumption about the X-rays, the behavior of the fast-decaying optical component cannot be reproduced as originating from a forward shock. The early optical decay index is $\alpha_F \approx 1.5$ if we fit a single component (no bump), though in our fits with a bump component the decay rate is steeper. (However, if we interpret the bump as a density variation or other modulation of a single power-law, rather than a truly separate component, the value of $\alpha_F \approx 1.5$ is most appropriate. For our discussion of the interpretation, we use the constraint $\alpha \gtrsim 1.5$, which is certainly true independent of the number of components used in our model.)

This decay is steeper than the $\alpha_X = 1.31$ decay slope observed in the X-ray at late times. In no regime of the forward-shock model can the longer-wavelength emission decay faster than X-rays at the same or later times (Sari et al. 1998).Further, the subsequent passage of ν_m or ν_c through the optical bands should produce breaks in the optical light curves which can only accelerate the temporal decay, not slow it.

The lack of flux excess in the first RAPTOR measurement, and the extrapolation of the Band model into the visible frequency range, argue against association with this emission to a prompt optical component from the internal shocks that (presumably) produced the high energy emission. Therefore, the most likely candidate to be responsible for this early optical emission is an external reverse shock which is produced when the forward shock begins to interact with the surrounding medium. Such an explanation has been previously used by several authors to explain observed peculiarities in the early light curves of a number of events (Sari & Piran 1999; Kobayashi & Zhang 2003; Shao & Dai 2005).

In the reverse shock scenario, electrons behind the forward shock are accelerated as the reverse shock propagates back through the relativistic ejecta. The mass density of this shell is higher than the density of the ISM swept up by the forward shock, resulting in a difference of a factor of roughly γ^2 between the random Lorentz factors of the forward and reverse shock electrons. Sari & Piran (1999) demonstrate that the frequency of the radiation emitted from a reverse shock should therefore differ from the forward shock by a factor of γ^2, peaking at optical frequencies. Starting with a similar argument and assuming that the reverse and forward shocks share the same magnetic field and bulk Lorentz factors at the moment they cross, Kobayashi (2000) derived that the temporal behavior of reverse shock light curves at frequencies $\nu_m < \nu < \nu_c$ can be given as $F_{\nu,r} \propto t^{3(2p-1)/2}$ for $t < t_{pk}$ and $F_{\nu,r} \propto t^{(-27p+7)/37}$ for $t > t_{pk}$ in the thin shell case, where t_{pk} represents the peak of the reverse shock emission. The observed light curve at frequencies $\nu < \nu_m$ will exhibit the

same rise profile, but will transition to a much slower post peak decline of $F_{\nu,r} \propto t^{-16/35}$ before transitioning to the faster $F_{\nu,r} \propto t^{(-27p+7)/37}$ decay.

The measured value of $\alpha_{F,av} \sim 1.52 \pm 0.02$ for the fast decay component (if the bump is ignored; steeper in the presence of a bump) essentially rules out the case in which $\nu < \nu_m$. If we use the X-ray inferred value of the electron power law index, $p = 2.00 \pm 0.14$, and apply it to the case where $\nu_m < \nu < \nu_c$, then the predicted reverse shock temporal decay is $\alpha_r \sim 1.74 \pm 0.12$, consistent within 2σ with our measured decay of α_F (or better if the bump is treated as separate, but we must then explain the origin of this bump). In this scenario, the break to a slower decay at 10^3 sec could be interpreted as the reverse-shock component giving way to the optical emission from the forward-shock. Of course, such an interpretation necessitates that the peak of the reverse shock emission occurred prior to the first RAPTOR observations some 20 seconds after the trigger. It would also require that the ν_m break of the forward shock have already passed through the optical band by the time of the transition from reverse to forward shock dominated emission.

In this model, the expected synchrotron spectrum during the decay portion of the reverse shock should follow $F_\nu \propto \nu^{-p/2}$, which for $p = 2.00 \pm 0.14$ would imply $\beta = 1.00 \pm 0.07$, the same as the late-time X-ray slope. This is only slightly shallower than the observed value of the fast-decaying component of $\beta_F \sim 1.25$ (corrected for Galactic extinction); the discrepancy may be due to a host-frame extinction. However, as we will discuss in §3.7, the lack of observable curvature in the SEDs of either the fast-decaying or the slow-decaying components impose strong constraints on the amount and nature of any extinction.

3.6. Physical Models of the Late-time Optical Light Curve

The fast-decaying early-time component is subsumed by the shallower late-time component at around 10^3 s. The natural inclination is to assume that the reverse shock emission has been replaced by that from a forward shock.

The initial fits to a single power-law during the slow decay strongly rule out a decay similar to the $\alpha_X \sim 1.3$ observed in the X-ray (or even the $\alpha_X \sim 1.0$ predicted by the adiabatic closure law) so the optical are unlikely to be in the same regime. For adiabatic evolution, if the optical is pre-cooling break (ISM-R), then a shallower decay is favored: for $p = 2.0$, we expect $\alpha_{opt} = 0.75$. This is consistent with the data, both in the empirical model where we assume a power-law that fades throughout the observations (for which we calculate $\alpha_S = 0.75 \pm 0.06$) and the more realistic fit in which the slow component rises, experiences a (chromatic) break, and then fades ($\chi^2/\mathrm{dof} = 228.0/197$ for this model, slightly better than the best model assuming an unbroken slow decay.) For radiative evolution and the case that the optical band is below the minimum-energy break (but above the cooling break and the critical frequency), $\alpha_{opt} = 4/7$, which is only consistent within 2.5σ.

If the slower decay component is due to the forward shock in which the optical band is in the range $\nu_m < \nu < \nu_c$ then the predicted intrinsic optical spectrum is $F_\nu \propto \nu^{-(p-1)/2}$, which for $p = 2.0 \pm 0.14$ suggests $\beta = 0.5 \pm 0.07$. If the forward shock is radiative, the prediction is the same but with no statistical uncertainty ($\beta = 1/2$). The observed spectral index of the possible forward shock component is somewhat redder than this value, $\beta_S = 0.92 \pm 0.08$ – or, using our physical model, the post-peak $\beta_S = 1.11 \pm 0.09$. Again, one may appeal to host extinction to make up the difference.

We will examine this possibility in greater detail in the next section. However, as was noted above, our measurement of the *change* in β between the fast and slow components is extinction-independent. For the empirical model with an unbroken slow component,

we measure a change $\Delta\beta_{F-S} = -0.38 \pm 0.08$; for the physical model the change is only $\Delta\beta_{F-S,b} = -0.12 \pm 0.08$ since the colors evolve back towards the red slightly after our observations, which occur near the best-fit peak time. The forward shock to reverse shock model predicts $\Delta\beta = 0.5$. This is consistent with our empirical model, though not with our best-fit physical model. This would imply that the forward shock peaked very early.

3.7. Broadband Spectral Fits and Constraints on Extinction

The light curve fits performed in our analysis naturally give rise to spectral fits. The filter-dependent flux parameters $F_{\nu,j}$ give the relative fluxes in each filter for both components of the light curve, and can be used to calculate the observed spectral energy distribution (SED) and look for signs of host extinction. We have already referred to the best-fit spectral indices β for the fast and slow components, all of which were fit assuming no host extinction. Here we will use different extinction models to constrain the properties of any host-frame dust in greater detail.

Large amounts of extinction are implied by the X-ray to optical SED. In Figure 10 we plot the SED of the second component (from the empirical, unbroken model) as computed at $t = 2000$ seconds, shortly before the end of our multi-filter observations and after the beginning of the XRT observations. Galactic extinction of $E(B-V) = 0.182$ has been corrected for. The predicted X-ray to optical slope, and the predicted slope in the optical-IR frequency window, is $\beta = (p-1)/2 = 0.5$ in the adiabatic case and also $\beta = 1/2 = 0.5$ in the radiative case, so the prediction is the same. In fact, however, we measure a nearly flat X-ray to optical slope of $\beta_{OX} = 0.23$ (using the R-band and 1 keV fluxes), and an IR-optical slope of $\beta_{opt} \sim 0.95$. This value of β_{OX} is enough to unambiguously label this event as a "dark burst" by the criterion of Jakobsson et al. (2004) (that is, any burst with β_{OX} less than the $p = 2$ synchrotron limit of 0.5) at this time, in spite of this being in fact

one of the optically brightest bursts ever observed by *Swift*! This surprising fact is owed to a combination of the unusual late X-ray brightness and the rapid early fading of the optical afterglow. (We could, perhaps, incorporate both this burst's early-time brightness and its later-time faintness with the moniker "grey burst", since "dark burst" seems inappropriate to the burst's entire evolution.)

The most commonly invoked interpretation for these dark bursts, and for X-ray/optical flux mismatches generally (e.g., Schady et al. 2007), is that the optical flux has been suppressed by dust extinction (or, for very high-redshift bursts, hydrogen absorption). A large amount of extinction would be necessary to apply this explanation here. To calculate a minimum amount of extinction, we assume the case that the cooling break (or for radiative evolution, the minimum-energy break) is just redward of the X-ray band, and take the minimum value of the intrinsic $\beta_{OX} = 0.43$ permitted by our uncertainty in β_X (this would imply $p < 2$, which is within our errors). For this case, the optical flux is overpredicted by a more than a factor of 5.3 in the observed V-band, requiring > 1.8 magnitudes of host extinction in this band, or $A_V = 1$ in the host-frame. This is an absolute minimum: requiring an intrinsic $\beta_{OX} = 0.5$ ($p = 2$ or a radiative regime) increases this to 2.2 magnitudes in the observed V, and placing the break at a more general point between the X-ray and optical bands increases it even further.

The X-ray spectrum displays evidence of a significant gas column density in excess of the Galactic value – using the host redshift of $z = 1.16$, we measure a best fit value of $N_{\rm H,host} = (1.1 \pm 0.3) \times 10^{22}$ cm^{-2}, compared to the Galactic estimate of $N_{\rm H,Galactic} = 0.103 \times 10^{22}$ cm^{-2}. This total observed N_H is greater than the Galactic N_H at $> 16\sigma$ significance.

Galactic extinction in this direction is $A_V = 0.56$, so assuming a Milky Way metallicity and extinction law we would anticipate a large host-frame extinction column of $A_V \approx 6$,

in fact greater than that indicated by the X-ray - optical discrepancy. For a more realistic choice of the gas-to-dust ratio in the SMC (about 8.4 times the Galactic value, from Gordon et al. 2003) or a starburst galaxy ($\sim$ 10 times Galactic, Lisenfeld et al. 2002) we expect a proportional reduction in A_V, predicting $A_V \approx 0.6 - 0.9$, roughly consistent with the minimum necessary suppression.

The wide frequency coverage, photometric accuracy, and contemporaneous nature of our optical data gives us the opportunity to firmly constrain the extinction properties of this event. As such, we fit a power-law plus an extinction component to our optical-IR SED, allowing the intrinsic unabsorbed spectral index β to vary as a free parameter. We try numerous extinction profiles: the Fitzpatrick & Massa ("FM") model (Fitzpatrick & Massa 1990), which has parameterizations for a wide range of galaxy types, of which we fit both a Milky Way extinction profile and a Small Magellenic Cloud profile using the parameters measured by Gordon et al. (2003). We also fit the Pei extinction profile (Pei 1992) for the Small Magellenic Cloud, and the Calzetti extinction profile (Calzetti et al. 2000) measured from observations of starburst galaxies. We use the flux parameters from our model of the slow component, and assume a systematic error of 2% in the IR filters, 3% in the optical filters, and 5% in U-band.

In every case, the best-fit model is that of no host-frame extinction ($A_V = 0$; our fits restrict A_V to be positive) or a very low value consistent with 0, indicating an intrinsic early-time spectral index equal to the observed spectral index of $\beta = 0.93 \pm 0.02$. This extinction-free fit is good, with $\chi^2/\mathrm{dof} = 1.91/6$, and is plotted in Figure 11.

The limit on A_V depends largely on the model adopted: greyer dust extinction models (and larger values of R_V, indicating larger grain sizes, within those models) permit more A_V. However, all "normal" dust models strictly limit the observed extinction to $A < 0.2$ in the observed V-band. The relatively grey Calzetti model allows more extinction, but even

for this case, the amount of observed extinction can only be achieved for ($R_V \gtrsim 8$) and the fit is degraded, $\chi^2/\mathrm{dof} = 4.70/6$ (Figure 11), though still acceptable. The χ^2 confidence contours for a few different fit models are plotted in Figure 12.

This is, furthermore, for the contrived "optimistic" case where the X-rays are just above the break - for the more general case where the break is at lower energy the required extinction is greatly increased. There is evidence to believe that this break is relatively near the optical at this time - the observations in the GCN circulars suggest a break around $t \approx 3 \times 10^4$ s, and despite some discrepancies all observations (including our single-epoch late-time PAIRITEL observations) agree that the optical flux by the second night has fallen well below the predicted value from the $\alpha < 1$ decay we measure at intermediate times. If we assume that this break in the light curve were due to a spectral break passing through the R-band, at $t = 2000$ seconds the break would be at ∼40 eV, predicting an optical flux 4 times (1.5 magnitude) higher even than the above "minimum" prediction would suggest, or 3.3 magnitudes total ($A_V \sim 1.8$ in the host frame.)

4. Discussion and Conclusions

Only with great contrivance does an approach using the assumptions of the standard model appear to explain all the features of this burst. Of course, one cannot rule out a model solely on the basis of contrivance. One possible implication might be that the dust properties around some gamma-ray bursts are so extreme that the extinction law is effectively grey (or more precisely, curvature-free), more so even than the Calzetti extinction model. Such a model is not entirely inconsistent with our data, and the large hydrogen column independently points us towards large amounts of extinction. Destruction of small dust grains by the intense radiation of the GRB might also aid in producing grey extinction laws. However, as our early-time optical data is a good fit to a power law this would have

to occur very quickly, and even for these very grey models our SED fits favor no extinction.

A second possibility is that there is an intrinsic break between the optical-IR and X-ray spectrum aside from the cooling break, and that the origins of the two forms of radiation are separate.

Any two-origin explanation must explain why the optical flux, whatever its origin, is not dominated by lower-energy emission from the peak region of the synchrotron spectrum that is generating the X-ray flux. This can be achieved by placing the minimum energy and cooling breaks at similar frequencies, so that the X-ray to optical index is $\beta = -1/3$ and the predicted optical flux is quite low. This is actually a case intermediate between the adiabatic ($\nu_m \ll \nu_c$) and radiative ($\nu_c \ll \nu_m$) models, and is not unreasonable for the standard range of physical afterglow parameters though it would require a value of the forward-shock Lorentz factor γ less than is usually assumed. Some extinction is likely required as well (unless $\nu_m \approx \nu_c \approx 500$ keV, which is a fairly contrived assumption), but as long as the amount is moderate we do not run into difficulties with contaminating the optical SED at the relatively early times of our observation. Later-time observations should hopefully be able to confirm or eliminate this possibility.

Of course, this model begs the question that if the optical afterglow is not due to the forward shock, what is its origin? The simplest possible answer is that the entire optical afterglow — early time and late time — has a single origin; perhaps the reverse shock. It is only our prior bias that leads us to try to associate some part of the optical light to the forward shock, but given that we have already associated much of the optical afterglow to the reverse shock it is not a great stretch to associate the rest of it with the same origin. The observed flattening may be just a very large "bump" comparable to that seen at very early times – this sort of interpretation would also better explain the GCN reports of steepening of the light curve at late times. Uhm & Beloborodov (2007) argue for a

reverse-shock dominated light curve and present simulated optical and X-ray light curves with bumps and shoulders resembling that seen in our data. However, they predict that the spectral index should generally evolve from blue to red across these features, which is the opposite of what we observe. (Even if this model were the correct one, however, the bright and long-lived X-ray afterglow would have to be associated with a different physical component.)

Alternatively, we can interpret the X-rays as being dominated by a non-synchrotron process. The lack of closure independently argues that the X-ray emission for this burst may not obey the normal assumptions about GRB afterglows. Inverse Compton emission may be involved, as was argued by Castro-Tirado et al. (2003) in the case of on GRB 030227, which displayed a similar discrepancy between its X-ray and optical properties.

As already noted, the very bright X-ray afterglow and late-time optical faintness are enough to qualify this event under some definitions of a dark gamma-ray burst in spite of the extraordinary bright early afterglow. Had the event been intrinsically fainter, at higher redshift, or had the optical follow-up been delayed significantly, the optical afterglow may have been missed entirely. Therefore, it is possible that events like GRB 061126 may represent a significant fraction of dark bursts. The most common interpretation of dark bursts is that they are due to absorption of the optical flux by host galaxy dust or by neutral hydrogen at very high redshift. However, unless the dust properties are truly exotic, our results suggest a third possibility: in some cases, the optical and X-ray fluxes are disconnected, possibly even not synchrotron.

In either case, we advise caution in interpreting future early afterglows in the absence of a truly complete data set. Many previous studies, by necessity, have been restricted in either their temporal properties (sampling), frequency coverage (available filters and wavebands), or both. Under the standard fireball model these assumptions seemed valid

as only a single parameter set would fit them. Here we show that when a more complete picture is available, *no* parameter set seems to fit the data, unless we invoke large quantities of grey dust or separate origins for the X-ray and optical afterglows.

The RHESSI team is supported by Swift AO-2 GI grant NNG06GH58G, "Completing Swift GRB Energy Spectra with Konus and RHESSI". We thank Kevin Hurley and Claudia Wigger for their support in acquiring and and analyzing these data. RAPTOR is primarily supported by Laboratory Directed Research and Development funding at Los Alamos National Laboratory. The Peters Automated Infrared Imaging Telescope (PAIRITEL) is operated by the Smithsonian Astrophysical Observatory (SAO) and was made possible by a grant from the Harvard University Milton Fund, the camera loan from the University of Virginia, and the continued support of the SAO and UC Berkeley. The PAIRITEL project and DP are further supported by NASA/Swift Guest Investigator Grant # NNG06GH50G. We thank M. Skrutskie for his continued support of the PAIRITEL project. KAIT was made possible by donations from Sun Microsystems, Inc., the Hewlett-Packard Company, AutoScope Corporation, Lick Observatory, the National Science Foundation, the University of California, the Sylvia & Jim Katzman Foundation, and the TABASGO Foundation. A.V.F.'s group at U.C. Berkeley is supported by NSF grant AST–0607485 and the TABASGO Foundation. Some of the data presented herein were obtained at the W. M. Keck Observatory, which is operated as a scientific partnership among the California Institute of Technology, the University of California, and NASA; the Observatory was made possible by the generous financial support of the W. M. Keck Foundation. We wish to extend special thanks to those of Hawaiian ancestry on whose sacred mountain we are privileged to be guests.

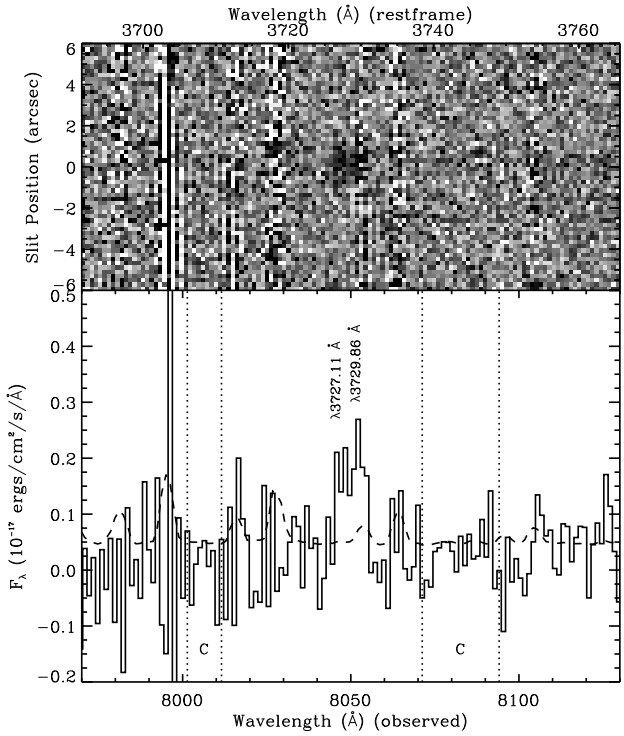

Fig. 3.— Spectrum of the host galaxy of GRB 061126 in the vicinity of the sole emission line, interpreted as the [O II] doublet. The data were taken with LRIS on Keck I using the 1″ slit and the 600/7500 grism. Top: Background subtracted, two-dimensional spectrogram showing the weighted mean of two 1200 second exposures. Pixels contaminated by cosmic rays in one exposure are excluded from the mean. Bottom: One-dimensional, coadded spectrum. The profile fit from a bright, nearby source was used to extract a spectrum at the known location of the GRB host galaxy. The dashed line represents the 1-sigma error at each pixel. The width of the emission feature is comparable to the spacing of the [OII] doublet at a redshift of 1.16. The doublet spacing is approximately equal to the instrument's resolution element at 805 nm, thus we expect the doublet to be barely resolved. We measure the galaxy's continuum by computing the median flux in two regions free of sky lines (regions "C"). Using this continuum value, and measuring the signal between 8042.0 and 8056.0 Å, we find that the total flux in this emission feature is $1.6 \pm 0.2 \times 10^{-17}$ erg s^{-1} cm^{-2}.

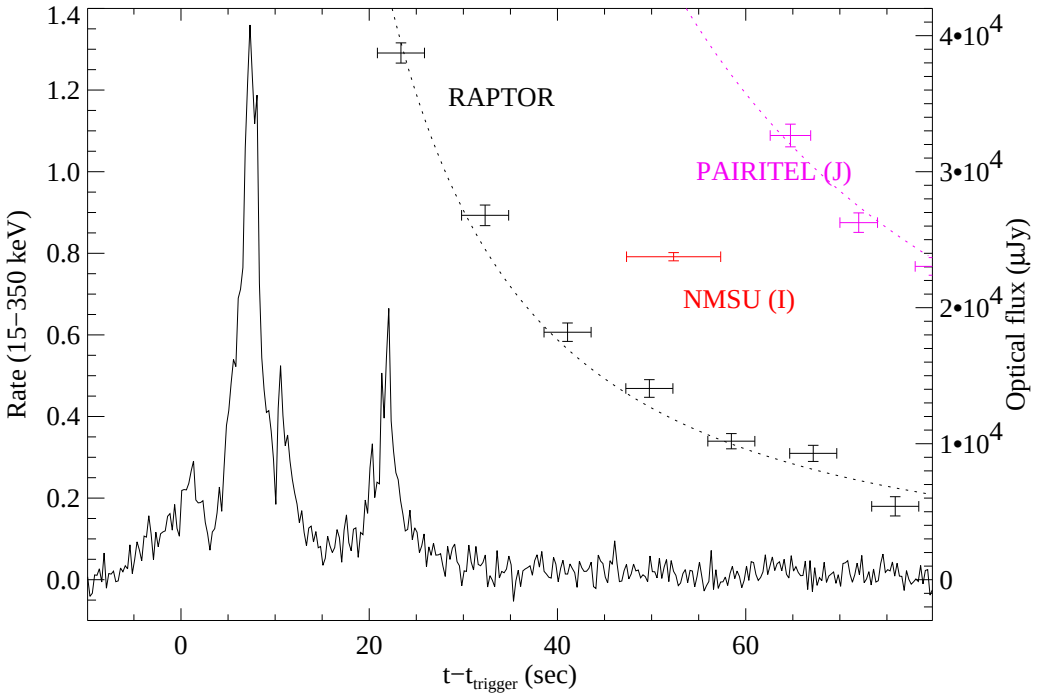

Fig. 4.— BAT 15-350 keV light curve of GRB 061126, showing the double-pulse profile of the main burst as well as the rapid response from the robotic telescopes RAPTOR, the NMSU 1.0m, and PAIRITEL. At this early time the light curves are well fit by a simple power-law ($F_\nu \propto t^{1.5}$) with t_o simply set to the trigger time. There is no evidence for a rising component or any correlation of the optical emission with the prompt emission.

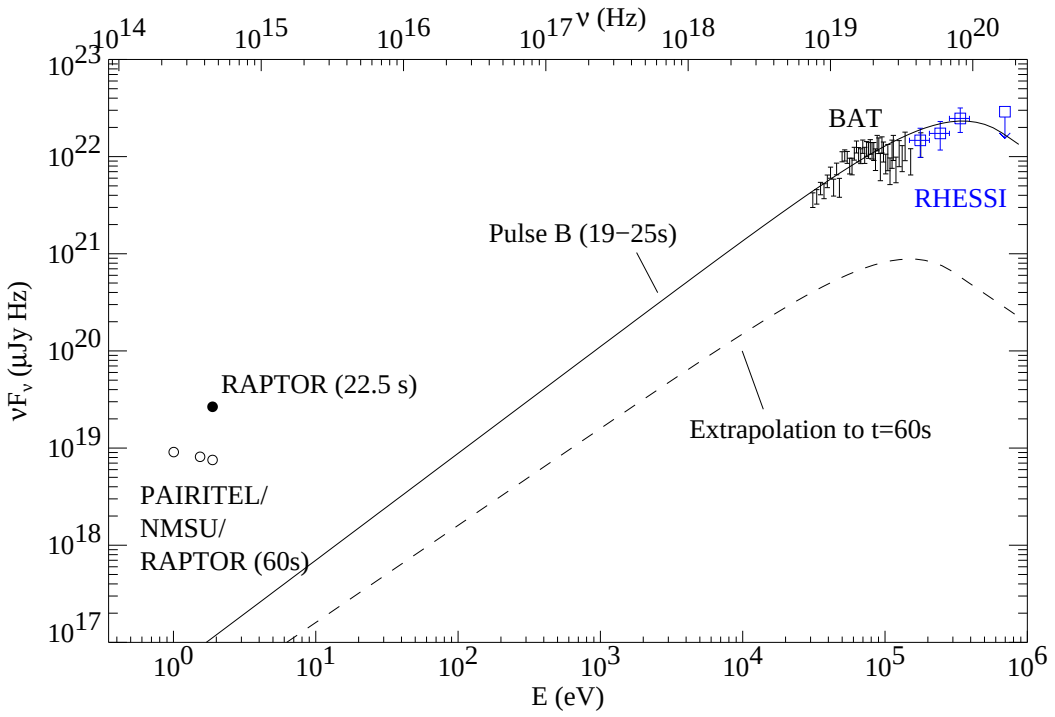

Fig. 5.— High-energy SED during the second pulse of the prompt emission (Pulse 'B'), with the contemporaneous RAPTOR measurement superimposed. An extrapolation of our best-fit Band model (Table 7) into the optical is shown to underpredict the optical flux by several orders of magnitude, suggesting that even at this very early time the optical afterglow is already present at 20 seconds post-trigger, dominating the early-time flux at long wavelengths. A temporal extrapolation of the BAT light curve to 60 seconds similarly underpredicts our multicolor data at that time.

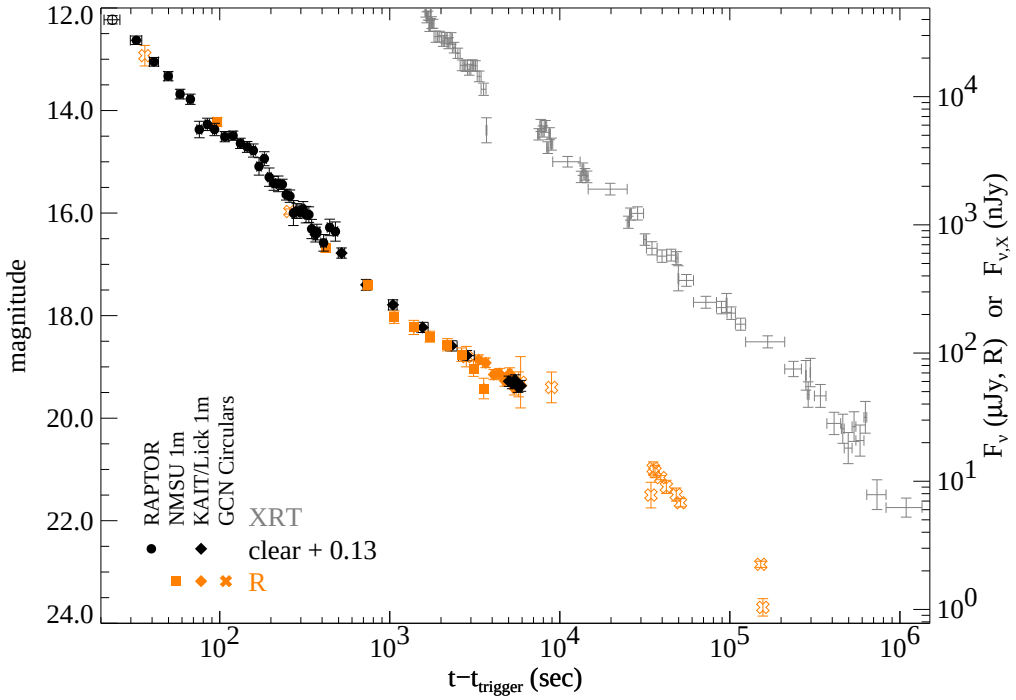

Fig. 6.— R-band and X-ray light curve of the afterglow of GRB 061126 showing the basic features of the early-to-late optical and X-ray afterglow light curves. Unfiltered data are also shown, offset by 0.13 magnitudes to match with the R-band calibration. Optical data are shown as filled (used in modeling) or unfilled (not used) symbols; X-ray data are shown as error bars with no central symbol. There is a rapid decay with a bump at early times, transitioning to a significantly slower decay that probably breaks at late times. Due to a delayed slew the X-ray afterglow was not observed until 1600s, but from then until it faded below the detection threshold at $\sim$ 9 days it decays as an unbroken power-law. The 1 keV normalized flux is plotted.

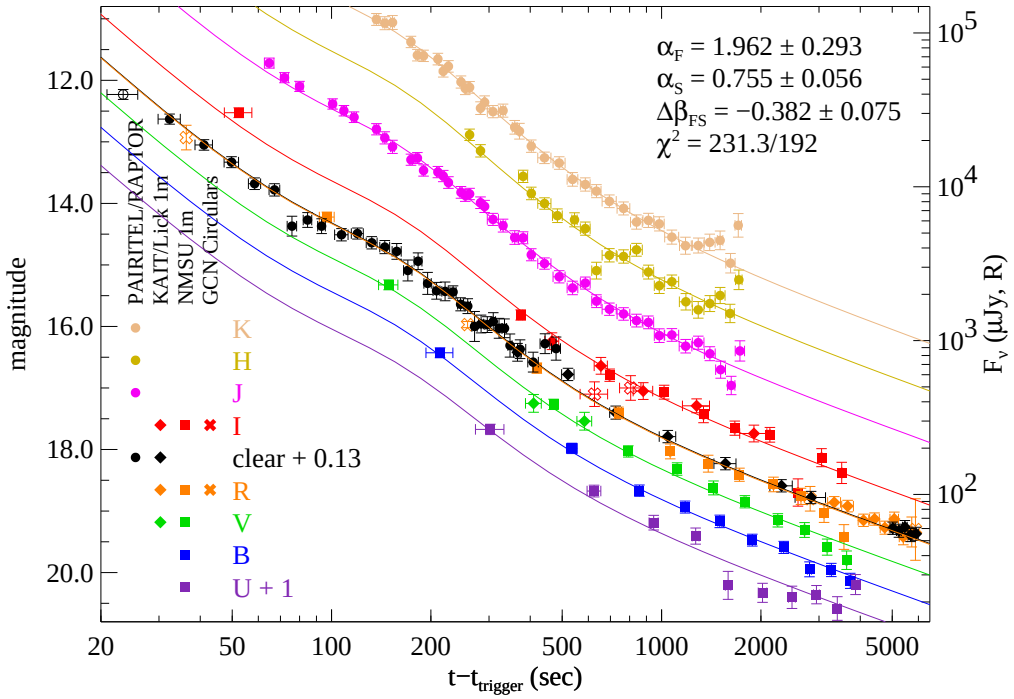

Fig. 7.— Broadband light curves of our early-time, multi-color photometry of the afterglow. The light curves are fitted with a three-component broken power-law model, assuming that the third component (with the slowest decay) has a spectral index that differs from the early component by an amount $\Delta\beta$.

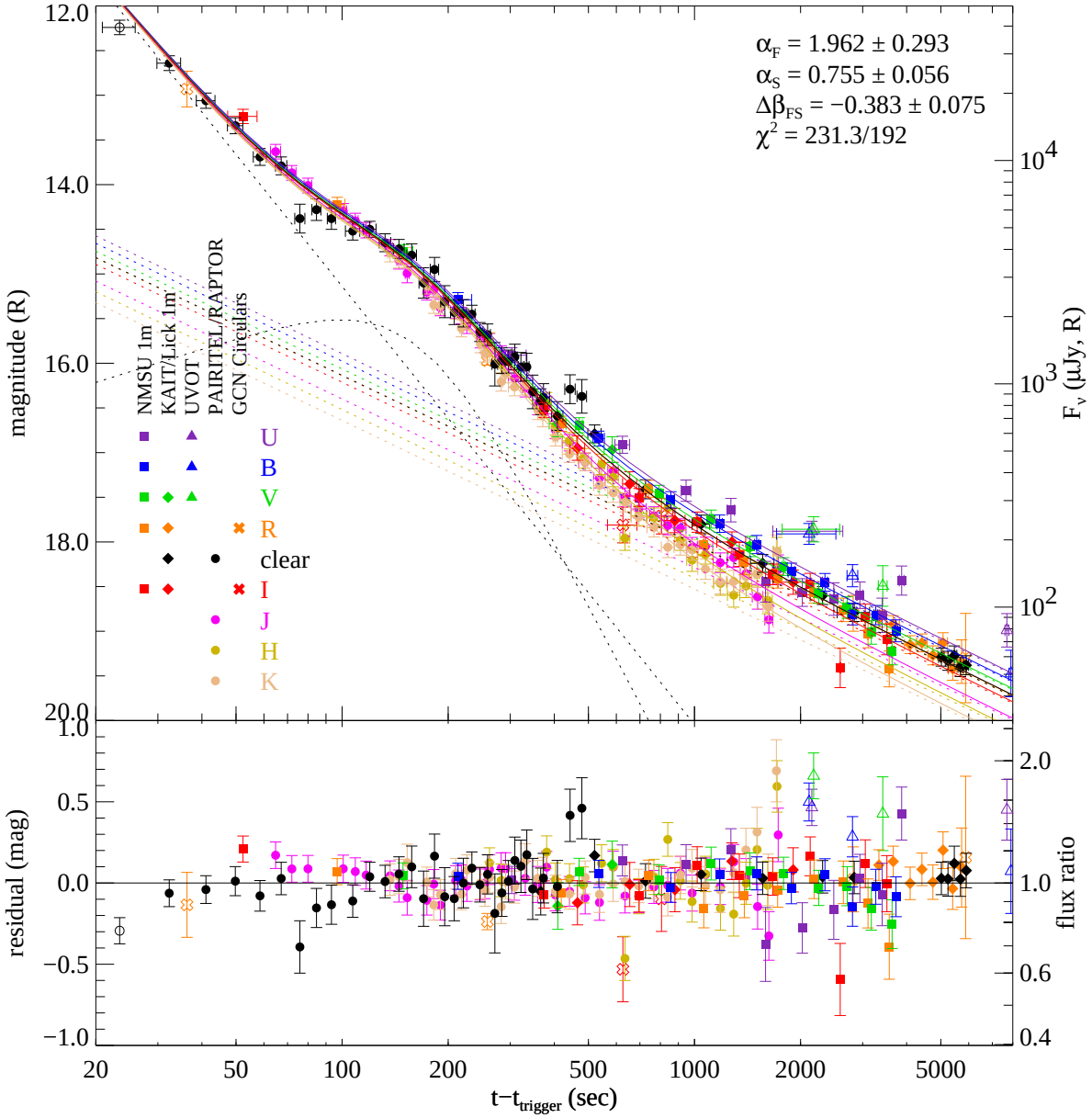

Fig. 8.— Broadband light curves of the afterglow with the curves aligned based on the early-time flux, emphasizing the red-to-blue color change. The model is the same as in Figure 7.

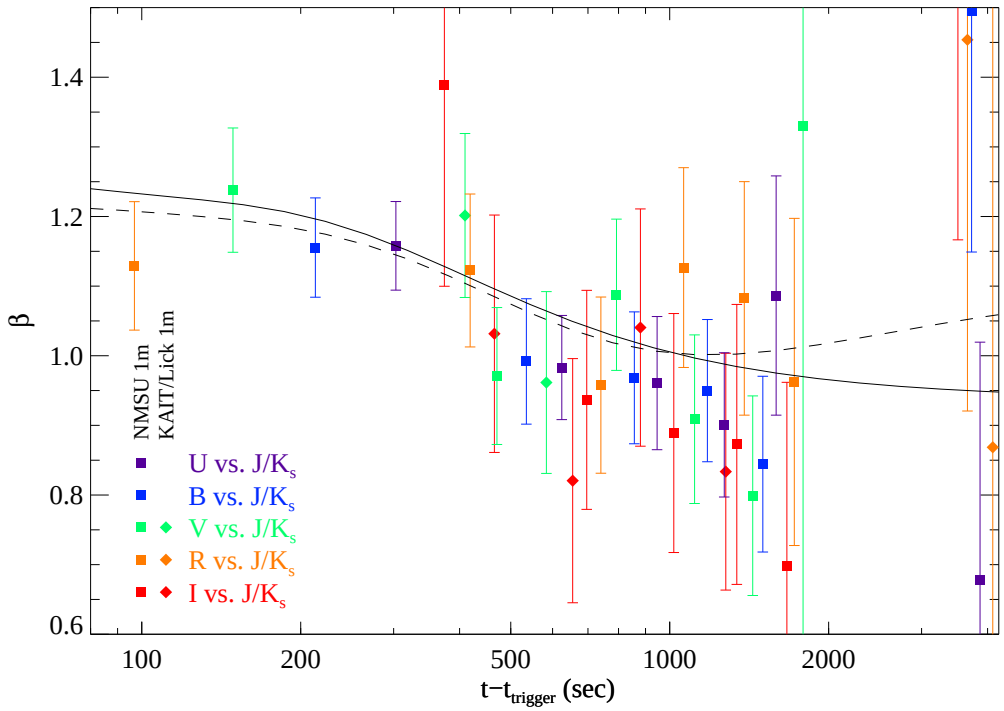

Fig. 9.— Evidence for color change across the transition from the fast-decaying component to the slow-decay component. We fit a power-law to simultaneous $J/H/K_s$ PAIRITEL exposures and optical exposures (in U, B, V, R, or I; color-coded appropriately) from the NMSU 1.0m telescope. The solid curves are not direct fits to these data, but represent the spectral index that would be observed at each time if fit to $K_s - U$ photometry based on two of our models. The solid line is for a model where the late-time component of the afterglow is modeled as a simple power-law; the dashed line represents a model of a forward shock undergoing a minimum-energy break at approximately the transition time.

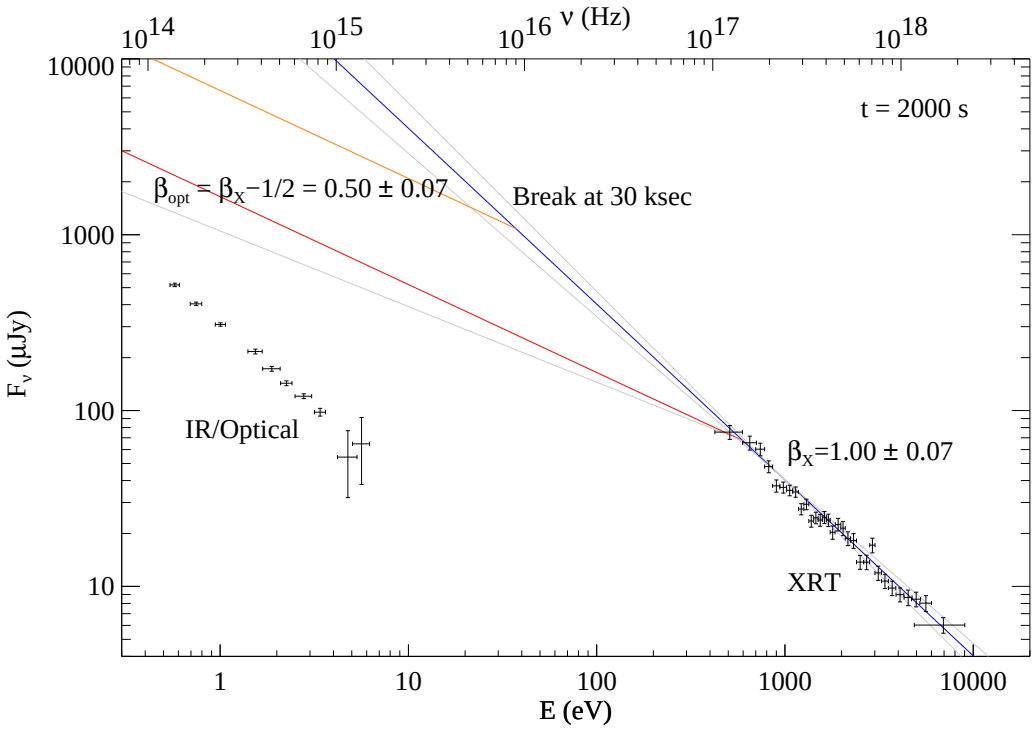

Fig. 10.— Broadband SED from optical to X-ray at $t = 2000$ seconds after the trigger. The steep X-ray decay and apparent shallow optical decay places the cooling break between the X-ray and optical bands. Even if we make the maximally generous assumption and place the cooling break at 1 keV, the optical flux is seen to be overpredicted (red line) by a factor of about 5. If we are less generous with our assumption, and choose to interpret the late-time break in the optical afterglow seen in the GCN circulars as the effect of the spectral break passing through the R-band at that time, the discrepancy is even larger. The optical data are a good fit to a power-law, and it is difficult to appeal to extinction to make up the difference.

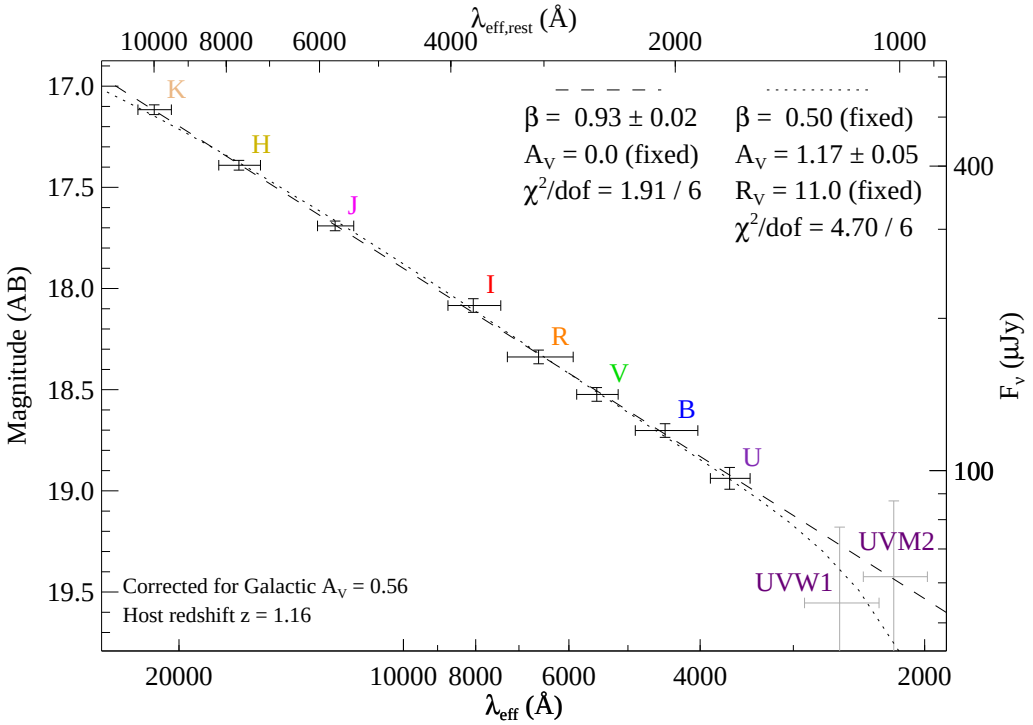

Fig. 11.— Spectral energy distribution of the slow-decaying component of the afterglow at 2000 seconds, fit both to a model assuming no host extinction (dashed line) and a model assuming host-frame extinction is present in sufficient quantity to provide the observed minimum discrepancy between these optical measurements and the X-rays. We use the Calzetti extinction model of starburst galaxies, with R_V in this case set very high, to 11. The uncertainties of the UVOT measurements are very large and we do not include them in our fits.

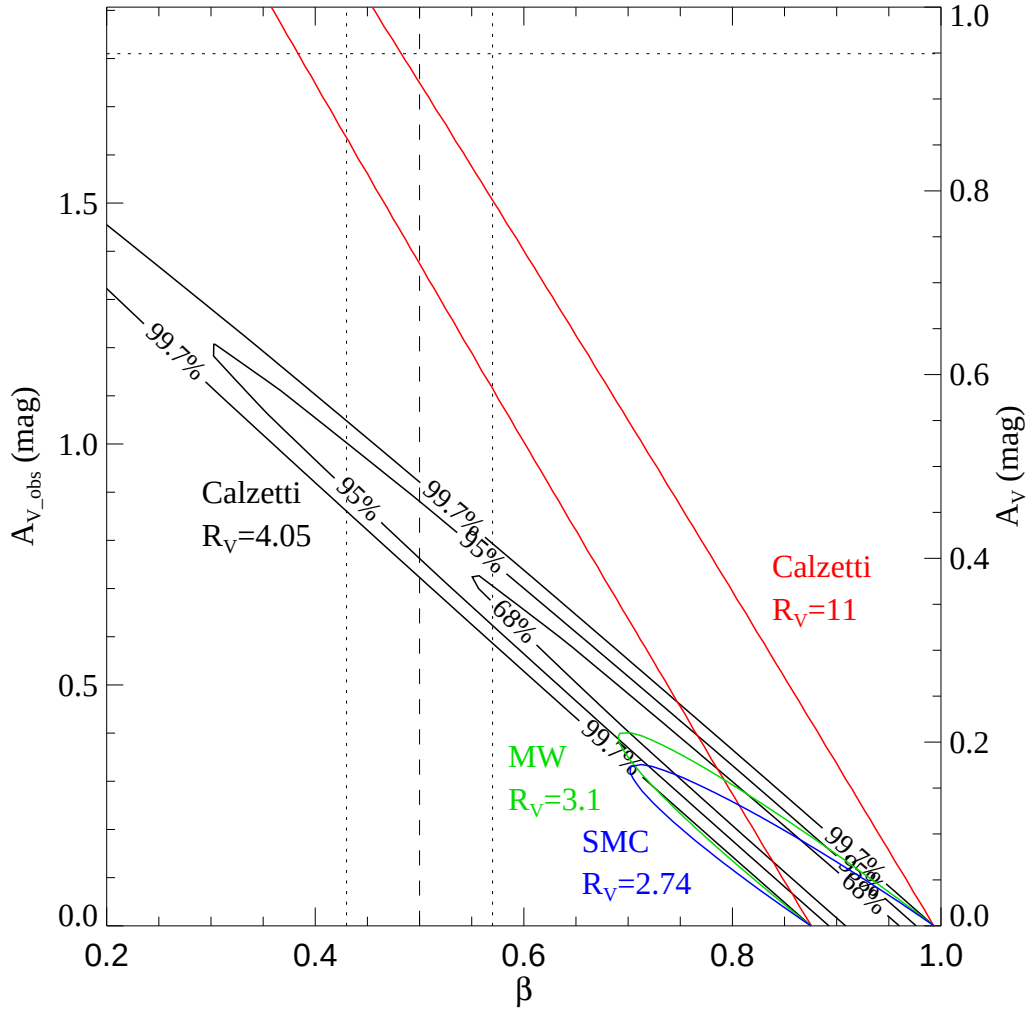

Fig. 12.— Plot of χ^2 as a function of A_V and the intrinsic unabsorbed β for different models. Extinction is strongly limited for standard extinction laws. The Calzetti extinction law allows slightly larger amounts of extinction, but still short of the amount required (an absolute minimum of 1.8 magnitudes, represented by the dotted line near the top). The vertical bars indicate the range of β predicted by the X-ray observations if the optical emission is due to a forward shock, though if the forward shock is still peaking the intrinsic β is allowed to be blueward (lower β) of this range.

REFERENCES

Akerlof, C., Balsano, R., Barthelmy, S., Bloch, J., Butterworth, P., Casperson, D., Cline, T., Fletcher, S., Frontera, F., Gisler, G., Heise, J., Hills, J., Kehoe, R., Lee, B., Marshall, S., McKay, T., Miller, R., Piro, L., Priedhorsky, W., Szymanski, J., & Wren, J. 1999, Nature, 398, 400

Amati, L., Frontera, F., Tavani, M., in't Zand, J. J. M., Antonelli, A., Costa, E., Feroci, M., Guidorzi, C., Heise, J., Masetti, N., Montanari, E., Nicastro, L., Palazzi, E., Pian, E., Piro, L., & Soffitta, P. 2002, A&A, 390, 81

Band, D., Matteson, J., Ford, L., Schaefer, B., Palmer, D., Teegarden, B., Cline, T., Briggs, M., Paciesas, W., Pendleton, G., Fishman, G., Kouveliotou, C., Meegan, C., Wilson, R., & Lestrade, P. 1993, ApJ, 413, 281

Barthelmy, S. D., Cannizzo, J. K., Gehrels, N., Cusumano, G., Mangano, V., O'Brien, P. T., Vaughan, S., Zhang, B., Burrows, D. N., Campana, S., Chincarini, G., Goad, M. R., Kouveliotou, C., Kumar, P., Mészáros, P., Nousek, J. A., Osborne, J. P., Panaitescu, A., Reeves, J. N., Sakamoto, T., Tagliaferri, G., & Wijers, R. A. M. J. 2005, ApJ, 635, L133

Beuermann, K., Hessman, F. V., Reinsch, K., Nicklas, H., Vreeswijk, P. M., Galama, T. J., Rol, E., van Paradijs, J., Kouveliotou, C., Frontera, F., Masetti, N., Palazzi, E., & Pian, E. 1999, A&A, 352, L26

Blake, C. H., Bloom, J. S., Starr, D. L., Falco, E. E., Skrutskie, M., Fenimore, E. E., Duchêne, G., Szentgyorgyi, A., Hornstein, S., Prochaska, J. X., McCabe, C., Ghez, A., Konopacky, Q., Stapelfeldt, K., Hurley, K., Campbell, R., Kassis, M., Chaffee, F., Gehrels, N., Barthelmy, S., Cummings, J. R., Hullinger, D., Krimm, H. A.,

Markwardt, C. B., Palmer, D., Parsons, A., McLean, K., & Tueller, J. 2005, Nature, 435, 181

Bloom, J. S. 2005, GCN Circular 4212

Bloom, J. S., Prochaska, J. X., Pooley, D., Blake, C. H., Foley, R. J., Jha, S., Ramirez-Ruiz, E., Granot, J., Filippenko, A. V., Sigurdsson, S., Barth, A. J., Chen, H.-W., Cooper, M. C., Falco, E. E., Gal, R. R., Gerke, B. F., Gladders, M. D., Greene, J. E., Hennanwi, J., Ho, L. C., Hurley, K., Koester, B. P., Li, W., Lubin, L., Newman, J., Perley, D. A., Squires, G. K., & Wood-Vasey, W. M. 2006a, ApJ, 638, 354

Bloom, J. S., Starr, D. L., Blake, C. H., Skrutskie, M. F., & Falco, E. E. 2006b, in ASP Conf. Ser. 351: Astronomical Data Analysis Software and Systems XV, ed. C. Gabriel, C. Arviset, D. Ponz, & S. Enrique, 751

Butler, N. R. & Kocevski, D. 2007, ArXiv Astrophysics e-prints

Calzetti, D., Armus, L., Bohlin, R. C., Kinney, A. L., Koornneef, J., & Storchi-Bergmann, T. 2000, ApJ, 533, 682

Castro-Tirado, A. J., Gorosabel, J., Guziy, S., Reverte, D., Castro Cerón, J. M., de Ugarte Postigo, A., Tanvir, N., Mereghetti, S., Tiengo, A., Buckle, J., Sagar, R., Pandey, S. B., Mohan, V., Masetti, N., Mannucci, F., Feltzing, S., Lundstrom, I., Pedersen, H., Riess, C., Trushkin, S., Vílchez, J., Lund, N., Brandt, S., Martínez Núñez, S., Reglero, V., Pérez-Ramírez, M. D., Klose, S., Greiner, J., Hjorth, J., Kaper, L., Pian, E., Palazzi, E., Andersen, M. I., Fruchter, A., Fynbo, J. P. U., Jensen, B. L., Kouveliotou, C., Rhoads, J., Rol, E., Vreeswijk, P. M., Wijers, R. A. M. J., & van den Heuvel, E. 2003, A&A, 411, L315

Christensen, L., Hjorth, J., & Gorosabel, J. 2004, A&A, 425, 913

Cool, R. J. 2006, GCN Circular 5985

Cool, R. J., Eisenstein, D. J., Hogg, D. W., Blanton, M. R., Schlegel, D. J., Brinkmann, J., Lamb, D. Q., Schneider, D. P., & Berk, D. E. V. 2006, GCN Circular 5863

Dai, Z. G. & Lu, T. 1999, ApJ, 519, L155

Dickey, J. M. & Lockman, F. J. 1990, ARA&A, 28, 215

Filippenko, A. V., Li, W. D., Treffers, R. R., & Modjaz, M. 2001, in ASP Conf. Ser. 246: IAU Colloq. 183: Small Telescope Astronomy on Global Scales, ed. B. Paczynski, W.-P. Chen, & C. Lemme, 121–+

Fitzpatrick, E. L. & Massa, D. 1990, ApJS, 72, 163

Gehrels, N., Chincarini, G., Giommi, P., Mason, K. O., Nousek, J. A., Wells, A. A., White, N. E., Barthelmy, S. D., Burrows, D. N., Cominsky, L. R., Hurley, K. C., Marshall, F. E., Mészáros, P., Roming, P. W. A., Angelini, L., Barbier, L. M., Belloni, T., Campana, S., Caraveo, P. A., Chester, M. M., Citterio, O., Cline, T. L., Cropper, M. S., Cummings, J. R., Dean, A. J., Feigelson, E. D., Fenimore, E. E., Frail, D. A., Fruchter, A. S., Garmire, G. P., Gendreau, K., Ghisellini, G., Greiner, J., Hill, J. E., Hunsberger, S. D., Krimm, H. A., Kulkarni, S. R., Kumar, P., Lebrun, F., Lloyd-Ronning, N. M., Markwardt, C. B., Mattson, B. J., Mushotzky, R. F., Norris, J. P., Osborne, J., Paczynski, B., Palmer, D. M., Park, H.-S., Parsons, A. M., Paul, J., Rees, M. J., Reynolds, C. S., Rhoads, J. E., Sasseen, T. P., Schaefer, B. E., Short, A. T., Smale, A. P., Smith, I. A., Stella, L., Tagliaferri, G., Takahashi, T., Tashiro, M., Townsley, L. K., Tueller, J., Turner, M. J. L., Vietri, M., Voges, W., Ward, M. J., Willingale, R., Zerbi, F. M., & Zhang, W. W. 2004, ApJ, 611, 1005

Ghirlanda, G., Ghisellini, G., & Lazzati, D. 2004, ApJ, 616, 331

Gordon, K. D., Clayton, G. C., Misselt, K. A., Landolt, A. U., & Wolff, M. J. 2003, ApJ, 594, 279

Jakobsson, P., Hjorth, J., Fynbo, J. P. U., Weidinger, M., Gorosabel, J., Ledoux, C., Watson, D., Björnsson, G., Gudmundsson, E. H., Wijers, R. A. M. J., Möller, P., Pedersen, K., Sollerman, J., Henden, A. A., Jensen, B. L., Gilmore, A., Kilmartin, P., Levan, A., Castro Cerón, J. M., Castro-Tirado, A. J., Fruchter, A., Kouveliotou, C., Masetti, N., & Tanvir, N. 2004, A&A, 427, 785

Kann, D. A. 2006, GCN Circular 5875

Kann, D. A. & Malesani, D. 2006, GCN Circular 5866

Kennicutt, Jr., R. C. 1998, ARA&A, 36, 189

Kobayashi, S. 2000, ApJ, 545, 807

Kobayashi, S. & Zhang, B. 2003, ApJ, 582, L75

Kouveliotou, C., Meegan, C. A., Fishman, G. J., Bhat, N. P., Briggs, M. S., Koshut, T. M., Paciesas, W. S., & Pendleton, G. N. 1993, ApJ, 413, L101

Li, W., Filippenko, A. V., Chornock, R., & Jha, S. 2003a, ApJ, 586, L9

—. 2003b, PASP, 115, 844

Li, W., Jha, S., Filippenko, A. V., Bloom, J. S., Pooley, D., Foley, R. J., & Perley, D. A. 2006, PASP, 118, 37

Lin, R. P., Dennis, B. R., Hurford, G. J., Smith, D. M., Zehnder, A., Harvey, P. R., Curtis, D. W., Pankow, D., Turin, P., Bester, M., Csillaghy, A., Lewis, M., Madden, N., van Beek, H. F., Appleby, M., Raudorf, T., McTiernan, J., Ramaty, R., Schmahl, E., Schwartz, R., Krucker, S., Abiad, R., Quinn, T., Berg, P., Hashii, M., Sterling, R.,

Jackson, R., Pratt, R., Campbell, R. D., Malone, D., Landis, D., Barrington-Leigh, C. P., Slassi-Sennou, S., Cork, C., Clark, D., Amato, D., Orwig, L., Boyle, R., Banks, I. S., Shirey, K., Tolbert, A. K., Zarro, D., Snow, F., Thomsen, K., Henneck, R., McHedlishvili, A., Ming, P., Fivian, M., Jordan, J., Wanner, R., Crubb, J., Preble, J., Matranga, M., Benz, A., Hudson, H., Canfield, R. C., Holman, G. D., Crannell, C., Kosugi, T., Emslie, A. G., Vilmer, N., Brown, J. C., Johns-Krull, C., Aschwanden, M., Metcalf, T., & Conway, A. 2002, Sol. Phys., 210, 3

Lipkin, Y. M., Ofek, E. O., Gal-Yam, A., Leibowitz, E. M., Poznanski, D., Kaspi, S., Polishook, D., Kulkarni, S. R., Fox, D. W., Berger, E., Mirabal, N., Halpern, J., Bureau, M., Fathi, K., Price, P. A., Peterson, B. A., Frebel, A., Schmidt, B., Orosz, J. A., Fitzgerald, J. B., Bloom, J. S., van Dokkum, P. G., Bailyn, C. D., Buxton, M. M., & Barsony, M. 2004, ApJ, 606, 381

Lisenfeld, U., Israel, F. P., Stil, J. M., & Sievers, A. 2002, A&A, 382, 860

Misra, K. 2006, GCN Circular 5903

Monet, D. G., Levine, S. E., Canzian, B., Ables, H. D., Bird, A. R., Dahn, C. C., Guetter, H. H., Harris, H. C., Henden, A. A., Leggett, S. K., Levison, H. F., Luginbuhl, C. B., Martini, J., Monet, A. K. B., Munn, J. A., Pier, J. R., Rhodes, A. R., Riepe, B., Sell, S., Stone, R. C., Vrba, F. J., Walker, R. L., Westerhout, G., Brucato, R. J., Reid, I. N., Schoening, W., Hartley, M., Read, M. A., & Tritton, S. B. 2003, AJ, 125, 984

Nousek, J. A., Kouveliotou, C., Grupe, D., Page, K. L., Granot, J., Ramirez-Ruiz, E., Patel, S. K., Burrows, D. N., Mangano, V., Barthelmy, S., Beardmore, A. P., Campana, S., Capalbi, M., Chincarini, G., Cusumano, G., Falcone, A. D., Gehrels, N., Giommi, P., Goad, M. R., Godet, O., Hurkett, C. P., Kennea, J. A., Moretti, A., O'Brien, P. T., Osborne, J. P., Romano, P., Tagliaferri, G., & Wells, A. A. 2006, ApJ, 642, 389

Nysewander, M. C., Reichart, D. E., Park, H.-S., Williams, G. G., Kinugasa, K., Lamb, D. Q., Henden, A. A., Klose, S., Kato, T., Harper, A., Yamaoka, H., Laws, C., Torii, K., York, D. G., Barentine, J. C., Dembicky, J., McMillan, R. J., Moran, J. A., Hartmann, D. H., Ketzeback, B., Bayliss, M. B., Bartelme, J. W., Crain, J. A., Foster, A. C., Schwartz, M., Holvorcem, P., Price, P. A., Canterna, R., Crew, G. B., Ricker, G. R., & Barthelmy, S. D. 2006, ApJ, 651, 994

Pei, Y. C. 1992, ApJ, 395, 130

Pozanenko, A., Shulga, A., Volnova, A., Ibrahimov, M., & Karimov, R. 2006, GCN Circular 5902

Price, P. A., Berger, E., Reichart, D. E., Kulkarni, S. R., Yost, S. A., Subrahmanyan, R., Wark, R. M., Wieringa, M. H., Frail, D. A., Bailey, J., Boyle, B., Corbett, E., Gunn, K., Ryder, S. D., Seymour, N., Koviak, K., McCarthy, P., Phillips, M., Axelrod, T. S., Bloom, J. S., Djorgovski, S. G., Fox, D. W., Galama, T. J., Harrison, F. A., Hurley, K., Sari, R., Schmidt, B. P., Brown, M. J. I., Cline, T., Frontera, F., Guidorzi, C., & Montanari, E. 2002, ApJ, 572, L51

Quimby, R. M., Rykoff, E. S., Yost, S. A., Aharonian, F., Akerlof, C. W., Alatalo, K., Ashley, M. C. B., Göğüş, E., Güver, T., Horns, D., Kehoe, R. L., Kızıloğlu, Ü., Mckay, T. A., Özel, M., Phillips, A., Schaefer, B. E., Smith, D. A., Swan, H. F., Vestrand, W. T., Wheeler, J. C., & Wren, J. 2006, ApJ, 640, 402

Rol, E., Wiersema, K., & Prema, P. 2006, GCN Circular 5876

Rykoff, E. S., Smith, D. A., Price, P. A., Akerlof, C. W., Ashley, M. C. B., Bizyaev, D., Garradd, G. J., McKay, T. A., McNaught, R. H., Phillips, A., Quimby, R., Schaefer, B., Schmidt, B., Vestrand, W. T., Wheeler, J. C., & Wren, J. 2004, ApJ, 601, 1013

Sari, R. & Esin, A. A. 2001, ApJ, 548, 787

Sari, R. & Piran, T. 1999, ApJ, 520, 641

Sari, R., Piran, T., & Narayan, R. 1998, ApJ, 497, L17

Sbarufatti, B., Barthelmy, S. D., Mangano, V., Page, K. L., Palmer, D. M., Stamatikos, M., & Berk, D. E. V. 2006a, GCN Circular 5855

Sbarufatti, B., Mangano, V., Guidorzi, G., Moretti, A., Stamatikos, M., Markwardt, C., Schady, P., Burrows, D., Barthelmy, S., Roming, P., & Gehrels, N. 2006b, GCN Reports, 16.2, GCN Report 16.2

Schady, P., Mason, K. O., Page, M. J., De Pasquale, M., Morris, D. C., Romano, P., Roming, P. W. A., Immler, S., & Vanden Berk, D. E. 2007, astro-ph/0702122

Schlegel, D. J., Finkbeiner, D. P., & Davis, M. 1998, ApJ, 500, 525

Shao, L. & Dai, Z. G. 2005, ApJ, 633, 1027

Skrutskie, M. F., Cutri, R. M., Stiening, R., Weinberg, M. D., Schneider, S., Carpenter, J. M., Beichman, C., Capps, R., Chester, T., Elias, J., Huchra, J., Liebert, J., Lonsdale, C., Monet, D. G., Price, S., Seitzer, P., Jarrett, T., Kirkpatrick, J. D., Gizis, J. E., Howard, E., Evans, T., Fowler, J., Fullmer, L., Hurt, R., Light, R., Kopan, E. L., Marsh, K. A., McCallon, H. L., Tam, R., Van Dyk, S., & Wheelock, S. 2006, AJ, 131, 1163

Smith, R., Melandri, A., Gomboc, A., & Bersier, D. 2006, GCN Circular 5857

Torii, K. 2006, GCN Circular 5868

Uhm, Z. L. & Beloborodov, A. M. 2007, astro-ph/0701205

Updike, A. C., Hartmann, D. H., Oswalt, T. D., & Rudkin, M. 2006, GCN Circular 5859

Vestrand, W. T., Wozniak, P. R., Wren, J. A., Fenimore, E. E., Sakamoto, T., White, R. R., Casperson, D., Davis, H., Evans, S., Galassi, M., McGowan, K. E., Schier, J. A., Asa, J. W., Barthelmy, S. D., Cummings, J. R., Gehrels, N., Hullinger, D., Krimm, H. A., Markwardt, C. B., McLean, K., Palmer, D., Parsons, A., & Tueller, J. 2005, Nature, 435, 178

Vestrand, W. T., Wren, J. A., Wozniak, P. R., Aptekar, R., Golentskii, S., Pal'Shin, V., Sakamoto, T., White, R. R., Evans, S., Casperson, D., & Fenimore, E. 2006, Nature, 442, 172

Vrba, F. J., Henden, A. A., Canzian, B., Levine, S. E., Luginbuhl, C. B., Guetter, H. H., Munn, J. A., Hartmann, D. H., & Jennings, M. C. 2000, ApJ, 528, 254

Williams, G. G. & Milne, P. A. 2006, GCN Circular 5869

Woźniak, P. R., Vestrand, W. T., Wren, J. A., White, R. R., Evans, S. M., & Casperson, D. 2006, ApJ, 642, L99

Yost, S. A., Swan, H. F., Rykoff, E. S., Aharonian, F., Akerlof, C. W., Alday, A., Ashley, M. C. B., Barthelmy, S., Burrows, D., Depoy, D. L., Dufour, R. J., Eastman, J. D., Forgey, R. D., Gehrels, N., Göğüş, E., Güver, T., Halpern, J. P., Hardin, L. C., Horns, D., Kızılovglu, U., Krimm, H. A., Lepine, S., Liang, E. P., Marshall, J. L., McKay, T. A., Mineo, T., Mirabal, N., Özel, M., Phillips, A., Prieto, J. L., Quimby, R. M., Romano, P., Rowell, G., Rujopakarn, W., Schaefer, B. E., Silverman, J. M., Siverd, R., Skinner, M., Smith, D. A., Smith, I. A., Tonnesen, S., Troja, E., Vestrand, W. T., Wheeler, J. C., Wren, J., Yuan, F., & Zhang, B. 2006, astro-ph/0611414

Table 1. RAPTOR Observations of GRB 061126

Δt[a] (sec)	Filter	Exp. Time (sec)	Magnitude[b]	Flux[b] (μJy)
23.4	clear	5.0	12.26 ± 0.01[c]	38725.8 ± 355.0
32.3	clear	5.0	12.66 ± 0.02	26791.7 ± 489.0
41.1	clear	5.0	13.08 ± 0.03	18197.0 ± 495.9

[a]Exposure mid-time, measured from the *Swift* trigger (UT 08:47:56.4)

[b]Observed value; not corrected for Galactic extinction

[c]Contemporaneous with strong GRB pulse; point not used in modeling.

Note. — Only the first three observations are. Additional data is available in the online supplement, or by request.

Table 2. PAIRITEL Observations of GRB 061126

Δt[a] (sec)	Filter	Exp. Time (sec)	Magnitude[b]	Flux[b] (μJy)
64.8	J	4.3	11.72 ± 0.02	32658.7 ± 507.4
262.0	H	4.0	12.89 ± 0.05	7177.9 ± 304.1
136.7	K_S	4.5	11.01 ± 0.05	26278.5 ± 1298.0

Note. — Only the first usable exposure in each band is given. The full table of photometry is available upon request, or in our online supplement.

[a]Exposure mid-time, measured from the *Swift* trigger (UT 08:47:56.4)

[b]Observed value; not corrected for Galactic extinction

Table 3. NMSU 1m Observations of GRB 061126

Δt[a] (sec)	Filter	Exp. Time (sec)	Magnitude[b]	Flux[b] (μJy)
52.3	I	10.0	12.53 ± 0.00	23746.5 ± 65.5
96.8	R	10.0	14.22 ± 0.01	6356.2 ± 35.0
148.8	V	20.0	15.32 ± 0.01	2737.8 ± 17.6
213.2	B	40.0	16.43 ± 0.01	1108.7 ± 9.2
302.9	U	60.0	16.67 ± 0.03	411.9 ± 9.4

Note. — Only the first filter cycle is given. Additional data is available in the online supplement, or by request.

[a]Exposure mid-time, measured from the *Swift* trigger (UT 08:47:56.4)

[b]Observed value; not corrected for Galactic extinction

Table 4. KAIT and Lick 1m Observations of GRB 061126

Δt[a] (sec)	Filter	Exp. Time (sec)	Magnitude[b]	Flux[b] (μJy)
366.0	clear	20.0	16.29 ± 0.12	946.2 ± 99.0
409.5	V	45.0	17.25 ± 0.12	464.5 ± 48.6
465.5	I	45.0	16.24 ± 0.11	776.2 ± 74.8
3336.0	R	300.0	18.86 ± 0.05	88.7 ± 4.0

Note. — R-band points are from the Lick 1m (Nickel) telescope; all others are from KAIT. Only the first exposure in each filter is given; additional data are available in the online supplement, or by request.

[a]Exposure mid-time, measured from the *Swift* trigger (UT 08:47:56.4)

[b]Observed value; not corrected for Galactic extinction

Table 5. UVOT Observations of GRB 061126

Δt[a] (sec)	Filter	Exp. Time (sec)	Magnitude[b]	Flux[b] (μJy)
2152.0	U	967.5	18.64 ± 0.11	67.1 ± 6.6
2114.0	B	809.5	19.05 ± 0.12	99.2 ± 10.1
2178.0	V	809.5	18.43 ± 0.14	156.5 ± 19.1
8862.0	V	902.0	20.51 ± 0.32	23.0 ± 5.8
7700.3	U	196.6	19.75 ± 0.19	24.2 ± 3.8
15119.5	U	295.1	20.33 ± 0.38	14.2 ± 4.2
2807.3	B	196.6	19.52 ± 0.12	64.4 ± 7.0
7905.3	B	196.6	20.61 ± 0.26	23.5 ± 5.0
3421.3	V	196.6	19.07 ± 0.23	87.2 ± 16.5

Note. — UVOT data points were not used in our light curve models. U, B, and V filter measurements are our own re-reductions. UV and White filter photometry are from GCN Report 16.2 (Sbarufatti et al. 2006b); they are not repeated here, but are also available in our online supplement.

[a]Exposure mid-time, measured from the *Swift* trigger (UT 08:47:56.4)

[b]Observed value; not corrected for Galactic extinction

Table 6. GCN Observations of GRB 061126

GCN no.	Δt[a] (sec)	Filter	Exp. Time (sec)	Magnitude[b]	Flux[b] (μJy)	Reference
5869	36.3	R	–	12.93 ± 0.20	20893.0 ± 3515.0	(1)
5857	258.3	R	–	15.97 ± 0.05	1270.6 ± 57.2	(2)
5868	626.4	I	120.0	17.10 ± 0.20	351.6 ± 59.1	(3)
5868	806.1	I	120.0	17.00 ± 0.20	385.5 ± 64.9	(3)
5859	2820.1	R	–	18.80 ± 0.20	93.8 ± 15.8	(4)
5859	5880.4	R	–	19.30 ± 0.50	59.2 ± 21.8	(4)
5859	8939.8	R	–	19.40 ± 0.30	54.0 ± 13.0	(4)
5866	34367.3	R	–	21.50 ± 0.25	7.8 ± 1.6	(5)
5876	152064	R	–	22.85 ± 0.06	2.2 ± 0.1	(6)
5875	156381	R	–	23.69 ± 0.17	1.0 ± 0.2	(7)
5902	39225.6	R	–	21.16 ± 0.04	10.7 ± 0.4	(8)
5902	51235.2	R	–	21.65 ± 0.08	6.8 ± 0.5	(8)
5903	35424.0	R	–	20.98 ± 0.10	12.6 ± 1.1	(9)
5903	36288.0	R	–	21.04 ± 0.09	11.9 ± 0.9	(9)
5903	42336.0	R	–	21.34 ± 0.10	9.0 ± 0.8	(9)
5903	48384.0	R	–	21.49 ± 0.10	7.9 ± 0.7	(9)

Note. — GCN data points were not used in our light curve models.

[a]Exposure mid-time, measured from the *Swift* trigger (UT 08:47:56.4)

[b]Observed value; not corrected for Galactic extinction

Note. — References. – (1) Williams & Milne 2006; (2) Smith et al. 2006; (3) Torii 2006; (4) Updike et al. 2006; (5) Kann & Malesani 2006; (6) Rol et al. 2006; (7) Kann 2006; (8) Pozanenko et al. 2006; (9) Misra 2006

Table 7. Results of Band (1993) model fits to the BAT+RHESSI spectrum of GRB 061126

Region	α	β	$E_{\rm peak}^{\rm obs}$ [keV]	100 keV Norm. [ph cm^{-2} s^{-1}]	χ^2_ν (DOF)
Full ($t = -6$–35s)	-1.06 ± 0.07	< -2.3	620^{+220}_{-160}	$7.8^{+0.7}_{-0.5} \times 10^{-3}$	0.733 (106)
Pulse A ($t = 3$–14s)	-0.94 ± 0.06	< -2.5	790^{+160}_{-130}	$1.8 \pm 0.1 \times 10^{-2}$	1.042 (105)
Pulse B ($t = 19$–25s)	$-0.9^{+0.2}_{-0.1}$	...	350^{+190}_{-110}	$1.1^{+0.4}_{-0.1} \times 10^{-2}$	1.179 (100)

Note. — Note.—The quoted errors correspond to the 90% confidence region. The data in each time region are acceptably fit by an exponential times powerlaw model. The high energy powerlaw component (with photon index β) is not required in the fits but can be constrained for regions "Full" and "Pulse A." Using $\alpha \approx -1$ and the declining $E_{\rm peak}$ and normalization values between pulses A and B, we estimate an approximately energy independent GRB spectral flux of $0.1^{+0.1}_{-0.5}$ mJy below 1 keV at $t = 60$s (Figure 5).

Table 8. X-ray closure relations

Model	ν_c	[b,c]	Closure	σ
ISM	B	[-3/2, 0]	-0.19 ± 0.11	1.78
	R	[-3/2, 1/2]	0.31 ± 0.11	2.87
Wind	B	[-3/2, -1/2]	-0.69 ± 0.11	6.44
	R	[-3/2, 1/2]	0.31 ± 0.11	2.87
Jet	B	[-2, -1]	-1.69 ± 0.14	11.83
	R	[-2, 0]	-0.69 ± 0.14	4.84

Note. — Results of closure relations fit to the X-ray data. None of the standard models gives better than 1.8σ consistency, and the only model accurate within 2σ predicts an unrealistically low circumburst density. Synchrotron self-Compton losses or a radiative evolution may be responsible.

Table 9. Summary of key parameters and χ^2 from the various models fit to the data. The model with no color change is strongly ruled out. The nature of the color change depends on the assumed model.

α_F	β_F	$\alpha_{S,b}$	$\alpha_{S,a}$	$\Delta\beta_{F-S}$	χ^2/dof
2.09 ± 0.29	1.28 ± 0.01	-	0.80 ± 0.05	-0.32 ± 0.03[a]	212.0/185
1.76 ± 0.22	1.07 ± 0.02	-	0.58 ± 0.12	0[b]	261.8/193
1.96 ± 0.29	1.31 ± 0.02	-	0.75 ± 0.06	-0.38 ± 0.08	231.3/192
1.70 ± 0.09	1.23 ± 0.02	-0.50[b]	0.75[b]	-0.12 ± 0.09[c]	227.6/197

[a]Not a formal fit parameter in this model - the flux amplitude parameters in each filter are allowed to assume their arbitrary best fit values. In other models the change in these parameters is constrained to be due to variation in the spectral index β.

[b]Fixed parameter.

[c]Change between the spectral index of the fast component and the index fit to the slow component after its peak ($\beta_{S,b}$). The slow component undergoes a chromatic break from $\beta_{S,b} = 0.284$ to $\beta_{S,b} = 1.11$.